

Multi-k magnetic structure and large anomalous Hall effect in candidate magnetic Weyl semimetal NdAlGe

C. Dhital^{1*,†}, R. L. Dally^{2,†}, R. Ruvalcaba³, R. Gonzalez-Hernandez⁴, J. Guerrero-Sanchez³, H. B. Cao⁵, Q. Zhang⁵, W. Tian⁵, Y. Wu⁵, M. D. Frontzek⁵, S. K. Karna^{6,7}, A. Meads¹, B. Wilson¹, R. Chapai⁷, D. Graf⁸, J. Bacsá⁹, R. Jin^{7,10}, and J.F. DiTusa^{7,11}

¹ *Department of Physics, Kennesaw State University, Marietta, GA, 30060, USA*

² *NIST Center for Neutron Research, National Institute of Standards and Technology, Gaithersburg, MD 20899-6102, USA*

³ *Centro de Nanociencias y Nanotecnología, Universidad Nacional Autónoma de México, Ensenada, BC 22860, México*

⁴ *Departamento de Física y Geociencias, Universidad del Norte, Barranquilla, Colombia.*

⁵ *Neutron Scattering Division, Oak Ridge National Laboratory, Oak Ridge, Tennessee 37831, USA*

⁶ *Department of Physics, Prairie View A&M University, Prairie View, TX, USA*

⁷ *Department of Physics, Louisiana State University, Baton Rouge, LA, 70803, USA*

⁸ *National High Magnetic Field Laboratory, Tallahassee, FL, 32310, USA*

⁹ *X-ray Crystallography Center, Department of Chemistry, Emory University, Atlanta, GA, 30322, USA*

¹⁰ *Center for Experimental Nanoscale Physics, Department of Physics and Astronomy, University of South Carolina, Columbia, SC, 290208, USA*

¹¹ *Department of Physics, The Purdue School of Science, IUPUI, Indianapolis, Indiana 46202, USA*

Abstract

The magnetic structure, magnetoresistance, and Hall effect of non-centrosymmetric magnetic semimetal NdAlGe are investigated revealing an unusual magnetic state and anomalous transport properties that are associated with the electronic structure of this non-centrosymmetric compound. The magnetization and magnetoresistance measurements are both highly anisotropic and indicate an Ising-like magnetic system. The magnetic structure is complex in that it involves three magnetic ordering vectors including an incommensurate spin density wave and commensurate ferrimagnetic state in zero field. We have discovered a large anomalous Hall conductivity that reaches $\approx 430 \Omega^{-1}\text{cm}^{-1}$ implying that it originates from an intrinsic Berry curvature effect stemming from Weyl nodes found in the electronic structure. These electronic structure calculations indicate the presence of nested Fermi surface pockets with nesting wave-vectors similar to the measured magnetic ordering

*Corresponding author: cdhital@kennesaw.edu

† These authors contributed equally to this work.

wavevector and the presence of Weyl nodes in proximity to the Fermi surface. We associate the incommensurate magnetic structure with the large anomalous Hall response to be the result of the combination of Fermi surface nesting and the Berry curvature associated with Weyl nodes.

1. Introduction

Weyl semimetals are characterized by linearly dispersing electronic bands near the Fermi surface and are classified into different types based on the degeneracies and distribution of nodes in momentum space [1,2]. The emergence of Weyl semimetal phases requires either broken space inversion symmetry or broken time-reversal symmetry [1–4]. When both symmetries are broken as in non-centrosymmetric magnetic compounds, then there is a possibility of tuning Weyl nodes using the coupling between topology and magnetism [5,6]. Materials having heavy rare earth elements are suitable for the study of intertwined electronic band topology and magnetism due to their penchant for long-range magnetic ordering, strong spin-orbit coupling, and low carrier density semi-metallic behavior. Recent studies on compounds belonging to RAIX (R=Rare earth, X=Si, Ge) have shown promising results suitable for the investigation of coupling between electronic topology and magnetism [7–10].

The RAIX family of materials has shown interesting magnetic orders and exciting electrical transport properties. The list of these properties includes Lorentz violating type II Weyl Fermions in LaAlGe [11], Fermi arcs and large anomalous Hall effect in PrAlGe [9,12,13], Kramers nodal lines in SmAlSi [14], singular magnetoresistance in CeAlGe [10,15], an intrinsic to extrinsic crossover in the anomalous Hall conductivity PrAlGe_{1-x}Si_x [16], and anisotropic anomalous Hall effect, magnetostriction effects, and Fermi arcs in CeAlSi [17,18]. The magnetic behaviors and magnetic structures also exhibit interesting variations including topologically non-trivial magnetic orders [8,9,12,17]. All these observations

indicate that this family of materials can be a productive place to search for exciting electronic and magnetic properties arising from the interplay of electronic topology and magnetism. With this motivation, we have investigated NdAlGe using magnetometry, electrical transport, neutron diffraction, and electronic structure calculations.

There are some recent magnetization and magnetotransport studies [19–22] performed on NdAlGe that indicate some of its magnetic properties are similar to sister compound NdAlSi [8], which hosts incommensurate magnetism mediated by Weyl fermions. The similarities between NdAlGe and NdAlSi include the non-centrosymmetric crystal structure, metamagnetic transition in-field, small value of saturation moment ($\approx 2.8 \mu_B$) compared to expected free ion (Nd^{3+}) moment value ($\approx 3.6 \mu_B$), and highly anisotropic magnetism. Despite many similarities, some differences were also reported in the same previous works. The main difference is the absence of an anomalous Hall effect in NdAlSi compared to the large anomalous Hall response in NdAlGe [19]. The other difference was the observation of two successive magnetic transitions in NdAlSi [8] but a single magnetic transition in NdAlGe [19–21]. Therefore, it is natural to ask why there are some key differences in the magnetic and anomalous Hall behavior between these two isostructural compounds with the same magnetic ion. The first step towards answering such questions is to understand the magnetic structures of these compounds. Although the magnetic structure of NdAlSi has been solved in a previous study [8], the magnetic structure of NdAlGe is still missing. In this work, we have solved the ground state magnetic structure of NdAlGe, and performed a systematic investigation correlating its magneto transport, and anomalous Hall response with its magnetic structure and electronic topology by employing neutron diffraction, magnetization, magnetotransport measurements, and electronic structure calculations. Our results

indicate that NdAlGe crystallizes in a non-centrosymmetric tetragonal structure with a space group ($I4_1md$) identical to other members of the $RAIX$ family [21,23–25]. We observed two successive magnetic transitions in dc magnetic susceptibility, heat capacity, resistivity, and the neutron order parameter at $T_{IC} = 6.3$ K and $T_C = 4.9$ K. These observations are similar to two transitions observed in NdAlSi [8] but differ from the recent observations [19,20] of single magnetic transition in NdAlGe. Our orientation-dependent magnetization and magnetoresistance measurements indicate a highly anisotropic Ising-like magnetic system in agreement with previous studies [19,20]. There is a non-monotonic variation of magnetoresistance which reaches up to 15% ($T = 0.4$ K, 18 T) for $H // c$ and 5% ($T = 0.4$ K, 18T) for $H \perp c$. It has an unusually high anomalous Hall response most likely originating from the intrinsic contribution from Berry curvature related to Weyl nodes near the Fermi surface. Our neutron diffraction measurements indicate an incommensurate ($\delta \approx 0.006$ r.l.u) ($T_C < T < T_{IC}$) to commensurate ($\delta = 0$) ($T < T_C$) magnetic order transition leading to a ground state defined by three magnetic wavevectors: $\mathbf{k}_0 = (0, 0, 0)$, $\mathbf{k}_1 = (\frac{2}{3}, \frac{2}{3}, 0)$ and $\mathbf{k}_2 = (\frac{1}{3}, \frac{2}{3}, 0)$. The ordered moment (vector sum of three magnetic structures) at 1.5 K is $2.85(1) \mu_B$ consistent with the bulk magnetization measurements. The Fermi surface shows nested hole pockets located at the magnetic ordering wavevector $\pm (\frac{1}{3}, \frac{1}{3}, 0)$ and Weyl nodes near the Fermi level. Thus, the magnetic behavior and magnetic structure of NdAlGe are similar to NdAlSi except for the fact that the quantum oscillations have not been observed in NdAlGe. The absence of quantum oscillations is most probably caused by the higher disorder as indicated by the residual resistivity ratio, $R_{RR} = 2.5$, and the low temperature resistivity, $\rho_{xx} = 23 \mu\Omega\text{-cm}$ at $T = 2$ K for crystals grown thus far. Our data, which demonstrate both the formation of incommensurate spin density wave and large anomalous Hall response, indicate that Weyl fermions are involved in forming the

magnetic order through the cooperative interplay between nested itinerant fermions and the RKKY interaction between local moments.

2. Experimental Details

Single crystals of NdAlGe were obtained using the flux method with excess Al serving as the flux. The elements were loaded in an alumina crucible in the ratio Nd: Ge: Al (1:2:20) and sealed inside a quartz tube under partial Ar pressure. The mixture was heated to 1100 °C in 4 hrs, homogenized at 1100 °C for 2 hrs then cooled to 700 °C at the rate of 8 °C/hr. The solution was subsequently centrifuged to obtain single crystals. The excess Al flux was removed using a NaOH: H₂O solution. The phase purity and crystallinity of the resulting crystals were probed using both powder and single crystal x-ray diffraction. Multiple single-crystal magnetic neutron diffraction experiments were performed at High Flux Isotope Reactor (HFIR) facility in Oak Ridge National Laboratory (ORNL) using the single crystal diffractometer HB-3A in four circles and two-axis mode, the Wide-Angle Neutron Diffractometer (WAND², HB-2C), the HB-1A triple-axis spectrometer, and the HB2A powder diffractometer. The experiment performed at HB-3A employed the four-circle mode with a closed-cycle refrigerator having a minimum temperature of 4.8 K. Subsequently, we employed this instrument in two-axis mode with a liquid helium cryostat having a minimum temperature of 1.5 K. Both experiments performed at HB-3A used a wavelength of 1.54 Å. Neutron experiments performed on the HB-2C WAND² diffractometer at Oak Ridge National Laboratory (ORNL) used a liquid helium cryostat with a minimum temperature of 1.5 K and a Ge (113) monochromator with a wavelength of 1.48 Å. Neutron experiments performed on the HB-1A triple-axis spectrometer at ORNL utilized a liquid helium cryostat with a minimum temperature of 1.5 K and a wavelength of 2.37 Å. Both a PG(002) monochromator and analyzer were used and Soller collimators before the monochromator, before the sample, after the sample, and before the detector was 40'

– 40' – 40' – 80', respectively. The sample was oriented in the $(H, K, 0)$ scattering plane. The neutron powder diffraction at HB-2A employed a neutron beam with a wavelength of 2.41 Å, defined by a Ge (113) crystal monochromator.

The magnetization measurements were carried out using Quantum Design Magnetic Property Measurement System (MPMS) at Louisiana State University (LSU) and National High Magnetic Field Laboratory (NHMFL) (SCM-5). The high-field magnetization measurements were carried out using cell 8 (35 T) at NHMFL. The magnetoresistance measurements were performed using four probe methods on a Quantum Design Physical Property Measurement System (PPMS) and an 18 T superconducting magnet (SCM-2) at NHMFL. Four electrodes were mounted on a single crystal sample using silver epoxies. The current was applied along the a -axis and the sample rotation angle was measured from the c -axis such that $\theta = 0^\circ$ corresponds to $H // c$ and $\theta = 90^\circ$ corresponds to $H // a \perp c$. Heat capacity measurements were performed at LSU using a PPMS. The magnetic field values are expressed in kOe (10 kOe = 1 T) units throughout this manuscript.

For the electronic structure calculations, we employed the plane wave pseudopotential implementation of DFT contained in the Vienna ab initio Simulation Package (VASP) [26–28]. The PBE-GGA [29] description of the exchange-correlation energy was employed. Relaxation of the atomic positions was carried out using the lattice parameters values: $a = b = 4.2270$ Å and $c = 14.6051$ Å. The convergence criterion for the total energy was set to 10^{-4} eV, paying special attention to keeping the I4₁md spatial symmetry in the system. A cutoff energy of 400 eV was set for the plane wave basis. A k -points grid of $5 \times 5 \times 5$ was used to discretize the first Brillouin zone, tripling it for the band structure calculations. This grid was generated using the Monkhorst-Pack method [30] and a Methfessel-Paxton [31] smearing of the second order with a width of 0.05 eV. We took into consideration the spin-orbit coupling (SOC) and Hubbard U corrections to account for the

relativistic effects and the highly correlated f -orbitals of the Nd atoms, respectively. The Hubbard corrective functional was set with an effective on-site Coulomb interaction of $U = 6$ eV on the f -orbital of the Nd atoms as used in previous studies [8,17] to improve the description of electronic correlation and localization. Calculations were performed using different permutations of these corrections (DFT, DFT+SOC, DFT+U, DFT+SOC+U), but only the results of the latter two are reported. The crystal structures, data processing, and graphs in this paper were generated using VESTA [32], VASPKIT [33], and Matplotlib [34] software, respectively. The Weyl nodes were determined using the Wannier Tools package [35] after an accurate interpolation of the FM band structure at the Fermi level with the Wannier 90 code [36].

Throughout the manuscript, error bars and uncertainties represent plus and minus one standard deviation.

3. Results

3. a Crystal Structure

Due to possible variations in the crystal structure of chemistry such as $\text{NdGe}_{2-x}\text{Al}_x$ and previous reports [37–39] which suggest a stoichiometry-dependent crystal structure, we performed crystal structure analysis employing different probes and different batches of samples. Powder x-ray diffraction was used to check for phase purity and single crystal x-ray diffraction, powder neutron diffraction, and single crystal neutron diffraction were employed to analyze the crystal structure. The results from single crystal x-ray diffraction, powder neutron diffraction, and single-crystal neutron diffraction are presented in Table I and appendix A. Both powder and single crystal samples are better refined with a non-centrosymmetric space group $I4_1md$ (#109) compared to centrosymmetric structure $I41/amd$ (#141). The

non-centrosymmetric space group is further confirmed by the value of Flack parameter being 0.02 ± 0.01 . The Flack parameter gives the absolute orientation of non-centrosymmetric crystal. The non-centrosymmetric structure ($I4_1md$) is an ordered structure of LaPtSi type where Ge and Al are ordered whereas the centrosymmetric structure is the disordered structure of type α -ThSi₂ where Al and Ge occupy the same site randomly with a 50:50 ratio [37]. Instead of a 1:1:1 ratio of Nd: Ge: Al, we also noticed some variations in stoichiometry for samples from different synthesis sets.

Table I: Results of crystal structure analysis using single crystal x-ray, neutron powder diffraction, and single crystal neutron diffraction. The difference in the goodness of refinement is presented. The Rietveld fittings are presented in Appendix A. Column II and III represent refinement of same data using two different space groups. The R-factor and RF factor are better for non-centrosymmetric group.

T = 173 K Single crystal x-ray Non-centrosymmetric	T = 20 K (Powder) Powder neutron Non-centrosymmetric	T = 20 K (Powder) Powder neutron Centrosymmetric	T = 4.8 K Single crystal neutron Non-centrosymmetric
Space group: $I4_1md$ a = 4.23076 (15) Å c = 14.6364(4) Å Z = 4 Reflections = 629 R (F ²) = 1.22 R ₁ = 0.027, wR ₂ = 0.032 Flack parameter = 0.02 ± 0.01	Space group: $I4_1md$ a = 4.2255(2) Å c = 14.6042(6) Å Z = 4 R-factor = 2.06 RF-factor = 1.62	Space group: $I4_1/amd$ a = 4.2274 (1) c = 14.6107 (4) Z = 4 R-factor = 6.5 RF-factor = 8.3	Space group: $I4_1md$ a = 4.224 (2) Å c = 14.624 (3) Å Reflections: 127 R-factor= 2.55 RF-factor = 3.77

3. b Magnetic Properties

The low field magnetic properties of NdAlGe are presented in Fig. 1. The magnetic properties are highly anisotropic with $(\chi_c/\chi_{ab})_{dc} = 83.6$ at $T = 2$ K as evident from Fig. 1a. The variation of *ac* susceptibility (Fig. 1b) shows a broad transition centered around 4.5 K, whereas the variation of *dc* susceptibilities for $H \parallel c$ (Fig. 1c) and $H \parallel a$ (Fig. 1d) with temperature indicate two possible magnetic transitions between $T_{IC} = 6.3$ K and $T_C = 4.9$ K. These transitions are more evident in heat capacity measurement presented in Fig 3.

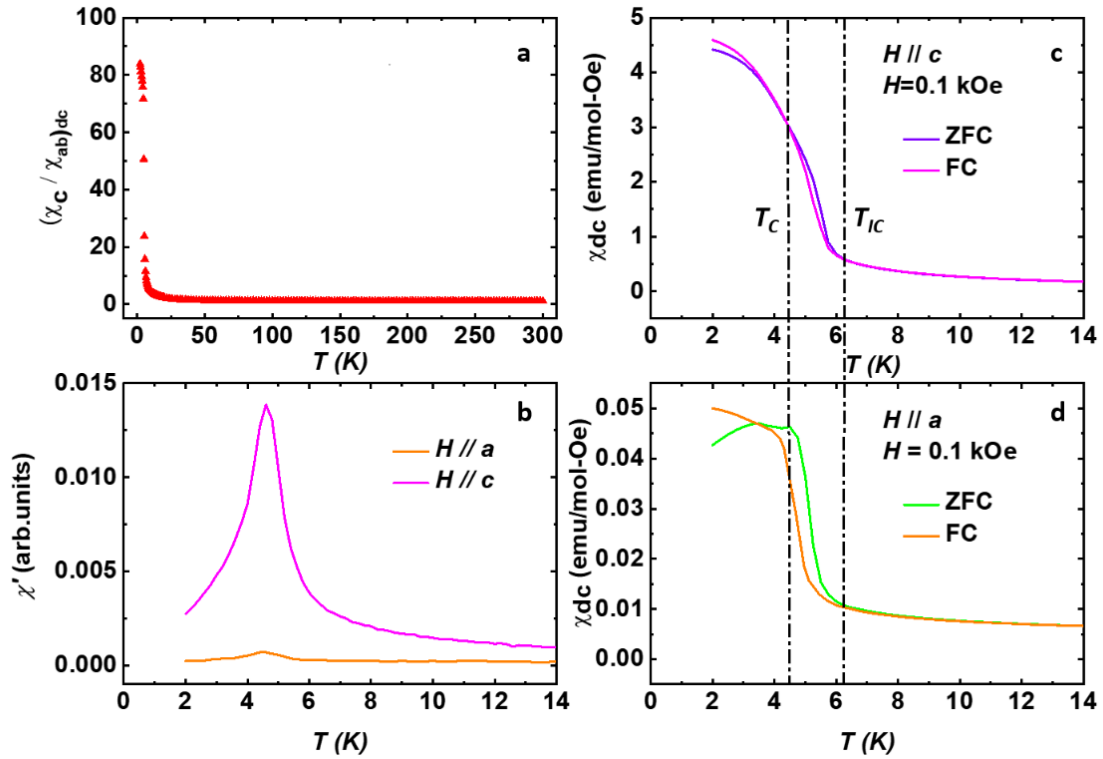


Fig. 1 *ac* and *dc* magnetic susceptibility measurements for NdAlGe. (a) The ratio of *dc* susceptibilities for $H \parallel c$, χ_c , and $H \parallel a$, χ_a , measured at $H = 0.1$ kOe (b) Variation of the real, χ' , and imaginary, χ'' , parts of the *ac* magnetic susceptibility with temperature, T , for $H_{ac} = 1$ Oe and $f = 20$ Hz. (c) Variation of zero field cooled (ZFC) and field cooled (FC) susceptibilities with T for $H \parallel c$ (d) Variation of (ZFC) and (FC) *dc* susceptibilities with temperature for $H \parallel a$ (1 emu/(mol Oe) = $4\pi \cdot 10^{-6}$ m³/mol).

For both field orientations ($H // c$ and $H // ab$), the susceptibility follows Curie-Weiss behavior $\chi(T) = \frac{C}{T - \theta}$, resulting in $\mu_{\text{eff}} = 3.42(3) \mu_B/\text{Nd}$, $\theta = +4.2(2) \text{ K}$ for $H // c$ and $\mu_{\text{eff}} = 3.59(5) \mu_B/\text{Nd}$, $\theta = -2.2 \text{ K}$ for $H // ab$. The effective moment μ_{eff} is slightly less than $3.66 \mu_B$ as expected for Nd^{3+} ion.

We also investigated the variation of the magnetization, M , as a function of the magnetic field, H . The results are presented in Fig. 2. We observe two distinct steps in the magnetization as a function of H for $T < T_C$. For $H // c$, the magnetization increases linearly and sharply until it reaches a magnetization plateau (shaded region I in Fig. 2a and b) at $M_1 = 0.95(5) \mu_B$ for $H_1 = 1 \text{ kOe}$. Here, the values of magnetization and field are defined for the center of the plateau and center of transition, respectively. With further increase in field, M remains relatively constant (5% change) until the field reaches 28 kOe (at $T = 2 \text{ K}$). With further increase in the field, there is a second stepwise increase in magnetization. The magnetization increases rapidly until the field reaches 44 kOe, and after that remains relatively constant (2% variation, shaded region II in Fig. 2a and b), reaching a value $M_2 = 2.8 \mu_B$ at 70 kOe at $T = 2 \text{ K}$. Here, the stepwise increase starts at 28 kOe and ends at 44 kOe so we define the midfield $H_2 = 36 \text{ kOe}$ as the second critical field. The value of H_1 remains constant between 2 K and 4 K, whereas the value of H_2 decreases with increasing temperature. Furthermore, the sharp increase in magnetization below H_1 is non-hysteretic (Fig. 2b) indicating the sharp increase is likely not due to domain alignment. The increase in magnetization near H_2 displays a small hysteresis (Fig. 2b) at $T = 2 \text{ K} < T_C$ but is non-hysteretic at $T = 5 \text{ K}$ between T_C and T_{IC} . Since, the value of M is less than that expected for localized Nd^{3+} ion for fields up to 70 kOe, we performed magnetization measurements up to 350 kOe for fields $H // c$ and $H // a$ as shown in Fig. 2c. The value of H_2 (115 kOe) for $H // a$ is much larger than the

value of H_2 (36 kOe) for $H // c$ reflecting a strong Ising-like magnetic anisotropy of the system. We also observed that the magnetization at $T = 1.8$ K and $H = 350$ kOe only reaches up to $2.81 \mu_B$ for $H // c$ and $2.2 \mu_B$ for $H // a$. These values are still significantly smaller than the expected free ion (Nd^{3+}) moment of $3.66 \mu_B$. This indicates the importance of itinerant magnetic moments to the magnetic state of this compound. In an itinerant ferromagnet, the small variation of dc magnetization in the field polarized phase generally originates from Pauli susceptibility of itinerant carriers.

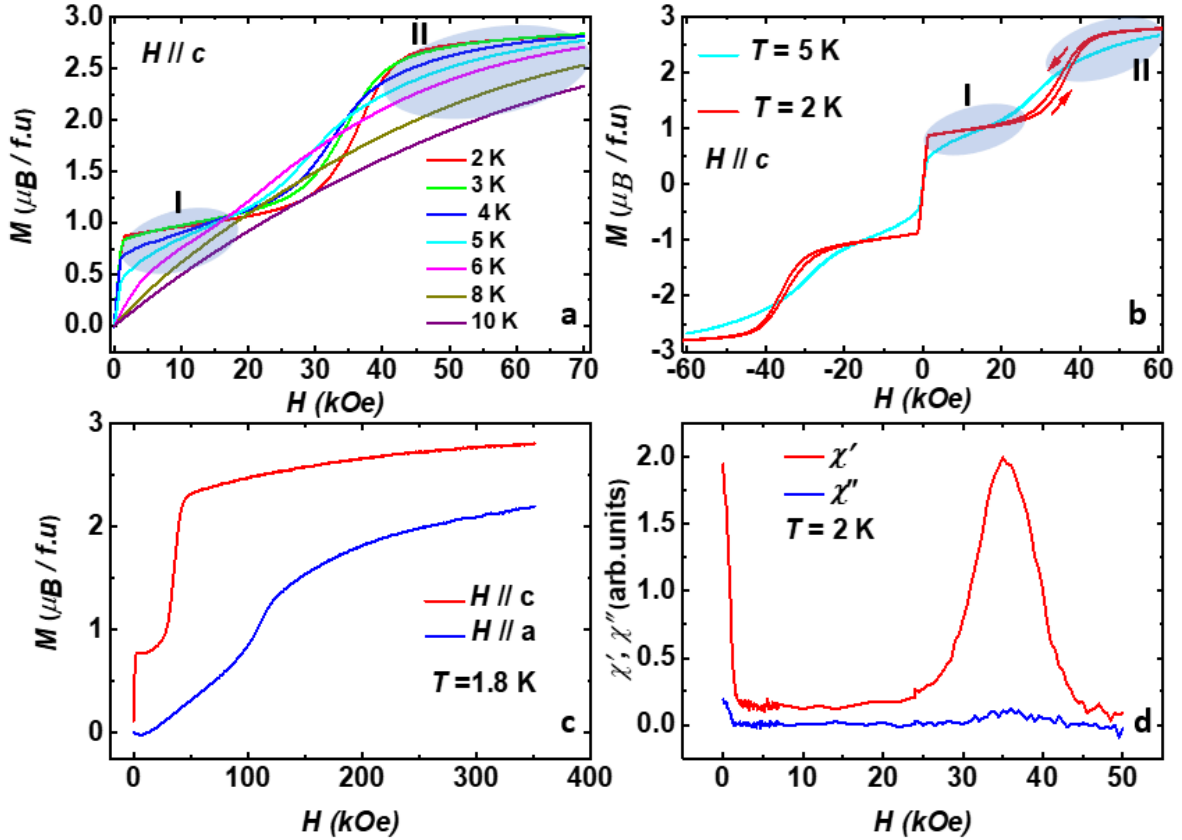


Fig.2 Magnetization of NdAlGe. (a) Magnetization, M , vs magnetic field, H , at select temperatures for $H // c$ (b) Hysteresis loop at 5 K and 2 K . The red arrows indicate increasing and decreasing fields at 2 K. The two plateau regions in magnetization are shaded and labeled as regions I and II (c) M vs H for $H // c$ and $H \perp c$ (d) Real part (χ') and imaginary part (χ'') vs H at $T = 2$ K with $H_{ac} = 1$ Oe and $f = 20$ Hz.

We have also investigated the field dependent dynamic behavior of M via *ac*-susceptibility measurements. Fig. 2d summarizes the results for $H \parallel c$, $H_{ac} = 2$ Oe and $f=100$ Hz. For $H < H_1$, there is a sharp decrease in χ' and χ'' followed by a peak near the metamagnetic transition H_2 ($=36$ kOe). These two features correspond to H_1 and H_2 as defined in *dc* magnetization measurements. The sharp decrease below H_1 is an indication of either domain alignment or the presence of non-collinear magnetic structure. The broad peak around H_2 is an indication of magnetic structure change due to spin reorientation. Both χ' and χ'' remain almost flat above 44 kOe when the system fully enters into field polarized phase.

3. c Specific Heat Capacity

We also measured the specific heat capacity of NdAlGe as a function of field and temperature. These are summarized in Fig. 3. Fig. 3a presents heat capacity as a function of temperature at select magnetic fields. There is a λ -anomaly near the magnetic transition temperature for fields $H \leq 10$ kOe as well as a Schottky-like anomaly centered around 17 K. A closer look at the region about the critical temperature reveals two distinct peaks (for $H = 0$) at $T_C = 4.9$ K and $T_{IC} = 6.3$ K (Fig 3b) indicating a sequence of two magnetic transitions. These two peaks merge for fields above H_1 , become broader above H_2 , and move to a higher temperature at higher magnetic fields indicating the possible mixing of crystal field levels. The zero-field heat capacity is fit with the Debye model [40](C_L) with the best fit found for $\theta_D = 240$ K (blue curve in Fig. 3b). The pink curve in Fig.3b represents the magnetic contribution to the specific heat $C_m = C_p - C_L$. The inset in Fig. 3b shows the variation of magnetic entropy: $Sm = \int_0^T \frac{C_m}{T} dT$ as a function of temperature. A total magnetic entropy of $R \ln 2$ just above T_{IC} and $0.93R \ln(10)$ is recovered between

2 K and 100 K indicating an $L = 6$, $S = 3/2$, $J = 9/2$ ground state of Nd^{3+} similar to NdAlSi [8].

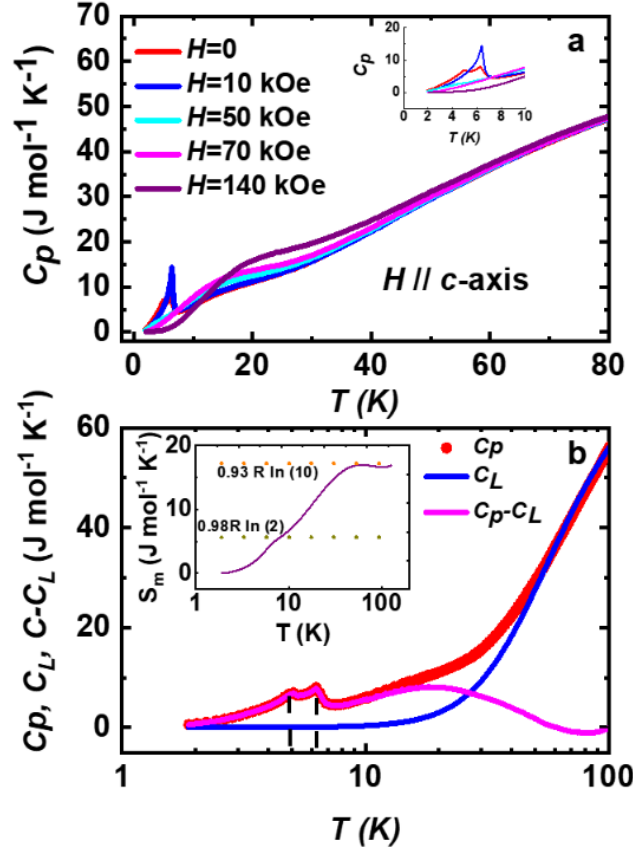


Fig.3 Specific Heat capacity of NdAlGe (a) Variation of specific heat capacity, C_p , with temperature, T , at select magnetic fields for $H // c$. Inset shows C_p below 10 K (b) Zero field heat capacity (red), fitted by the Debye model, C_L (blue), magnetic component to specific heat, $C_m = C_p - C_L$, and magnetic entropy, S_m (inset) as a function of temperature, T .

3.d Magnetoresistance and Hall Effect

We also performed resistivity measurements in magnetic fields up to 180 kOe (18 T) for different orientations of the magnetic field to explore the charge degrees of freedom and the influence of the magnetic ordering. The variation of resistivity with temperature is shown in Fig 4a and in Appendix B. The resistivity, ρ_{xx} , decreases monotonically (See Appendix B) from $T = 300$ K to $T_{IC} = 6.3$ K. The resistivity

displays anomalies at both $T_{IC} = 6.3$ K and $T_C = 4.9$ K. Such non-monotonic variation can arise either due to a reduction in carrier density due to the formation of incommensurate spin density wave (SDW) state [41,42] or due to enhanced scattering from domain walls or from the critical magnetic fluctuations. Below T_C , the resistance drops sharply due to a reduction in spin disorder scattering. Fig. 4b presents the magnetoresistance of NdAlGe at temperatures between 2 K and 10 K for fields up to $H = 90$ kOe for $\theta = 0^\circ$ ($H // c$ -axis). For $T < T_C$, the magnetoresistance is positive up to the metamagnetic transition at H_2 . At H_2 , the magnetoresistance drops significantly and then increases at higher field. The decrease in resistance at H_2 may be ascribed to the formation of a polarized magnetic state and reduction in spin disorder scattering. For $T_C < T < T_{IC}$ (i.e. at 5 K and 6 K), the magnetoresistance decreases sharply around $H = 0$ (shaded area in Fig. 4b) and then increases again for fields above H_1 . This indicates that the zero-field magnetic structure between T_C and T_{IC} is different than that below T_C . To investigate the possibility of observing quantum oscillations and the variation of magnetoresistance above H_2 , we also performed orientation and field-dependent magnetoresistance measurements up to 180 kOe using the superconducting magnet SCM-2 at NHMFL. The results are presented in Fig. 4c. The magnetoresistance peaks near H_2 and increases monotonically for $H > H_2$ reaching up to 15% at $T = 0.4$ K and $H = 180$ kOe for $H // c$ ($\theta = 0^\circ$). A large positive magnetoresistance in the field-polarized magnetic state ($H > H_2$) is rather counterintuitive and cannot be simply described by the Lorentz contribution. This implies the possibility of Fermi surface reconstruction as suggested for NdAlSi [43] and other f -electron compounds [44]. Unfortunately, we did not observe quantum oscillations in measurements of the resistivity. The inherent disorder present in our sample ($R_{RR} = 2.5$) is likely the cause and does not allow a validation of a scenario of changing the Fermi surface topology. We also observed that the value of H_2 increases monotonically with θ at the same time the

magnetoresistance decreases with θ . This is expected in a magnetically anisotropic system where the spins are primarily oriented along the c -axis.

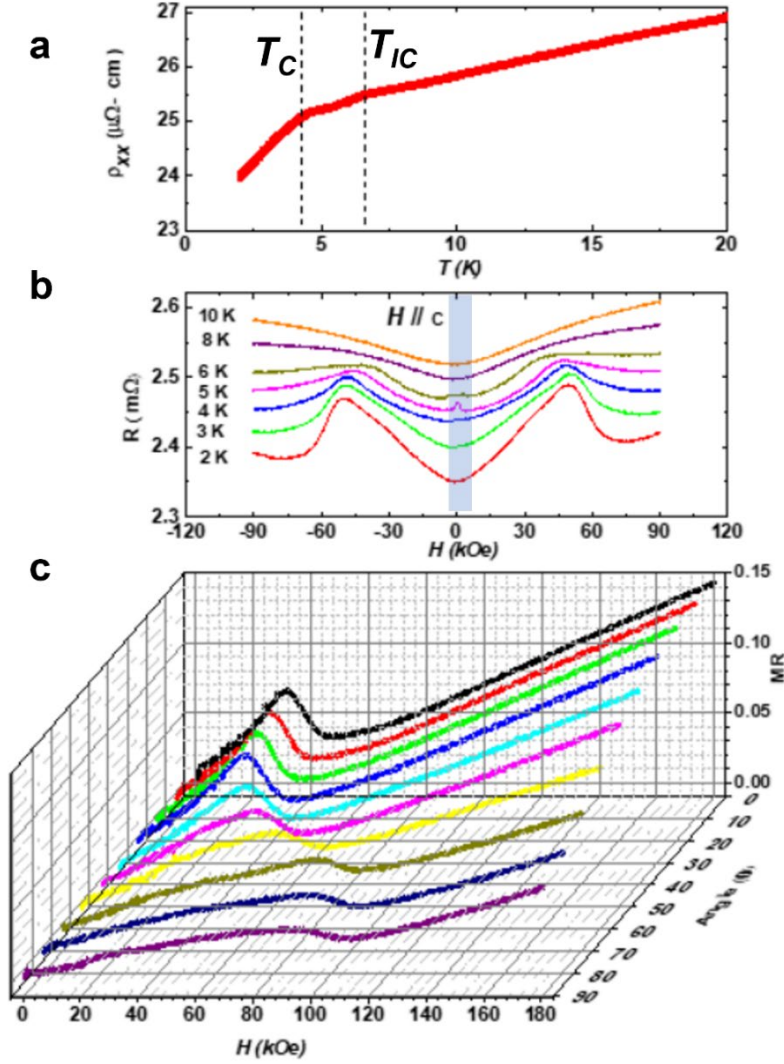


Fig. 4 Magnetotransport behavior of NdAlGe. (a) Variation of zero field resistivity, ρ_{xx} , with temperature, T . (b) Variation of resistance, R , with the magnetic field, H , at different temperatures for $H // c$ (c) Variation of magnetoresistance, MR ($MR = \frac{R(H) - R(0)}{R(0)}$), with the magnetic field, H for different orientations of the magnetic field at $T = 0.4$ K.

We have also measured the Hall effect for NdAlGe with the results are presented in Fig. 5. The symmetrized Hall resistivity, ρ_{xy} plotted as a function of H in Fig. 5a, interestingly exhibits two regions with different slopes for $T \leq T_{IC}$. These two regions are more clear in the inset of Fig.5a. These two regions correspond to two different

plateaus (I and II) observed in magnetization measurements in Fig. 2a and 2b. The data in Fig. 5a can be fitted (for $T \leq T_{IC}$) with two straight lines using the relation: $\rho_{xy} = R_0 H + \rho_{xy}^A$ [45,46], where the slope R_0 is the ordinary Hall coefficient and the intercept ρ_{xy}^A gives the anomalous Hall resistivity. The anomalous conductivity, σ_{xy}^A can then be calculated using the relation: $\sigma_{xy}^A = \frac{\rho_{xy}^A}{(\rho_{xy}^A)^2 + (\rho_{xx})^2}$. From the two different intercepts in $T \leq T_{IC}$, we estimated large values of σ_{xy}^A to be $|\sigma_{xy}^{A, I}| \approx 430 \Omega^{-1} \text{ cm}^{-1}$ and $|\sigma_{xy}^{A, II}| \approx 1020 \Omega^{-1} \text{ cm}^{-1}$, respectively, at $T = 2 \text{ K}$. These values decrease to $|\sigma_{xy}^{A, I}| \approx 170 \Omega^{-1} \text{ cm}^{-1}$ and $|\sigma_{xy}^{A, II}| \approx 530 \Omega^{-1} \text{ cm}^{-1}$, respectively, at $T = 6 \text{ K}$. To take into account the variation of magnetization and resistivity with temperature, we also analyzed the variation of $\frac{\rho_{xy}}{H}$ with $\frac{M}{H}$ at different temperatures. Fig. 5b shows the variation of $\frac{\rho_{xy}}{H}$ with $\frac{M}{H}$ at different temperatures. Each temperature dataset for $T \leq T_{IC}$ in Fig. 5b can be divided into two linear regions (Inset of Fig. 5b) corresponding to two plateaus (I and II) in magnetization data. For $T > T_{IC}$, the straight region corresponding to the lower plateau (region I) disappears and can be fit with a single straight line in the high field region (plateau II). The linear region in $\frac{\rho_{xy}}{H}$ vs $\frac{M}{H}$ can be modelled using the equation for Hall resistivity: $\frac{\rho_{xy}}{H} = R_0 + 4\pi R_S \frac{M}{H}$. In this equation, the intercept, R_0 , represents the ordinary Hall coefficient which in the simplest model is $1/ne$ where n is the carrier density and e is the electronic charge. The slope, $4\pi R_S$, provides the anomalous Hall coefficient, R_S . For $T \leq T_{IC}$, fitting of straight lines in regions I (4 kOe-20 kOe) and II (46 kOe-70 kOe) gives two values of R_S , i.e. R_S^I and R_S^{II} . The intercept R_0 is the same (within error) for the two regions. For $T \geq T_{IC}$, only the region with a slope R_S^{II} survives.

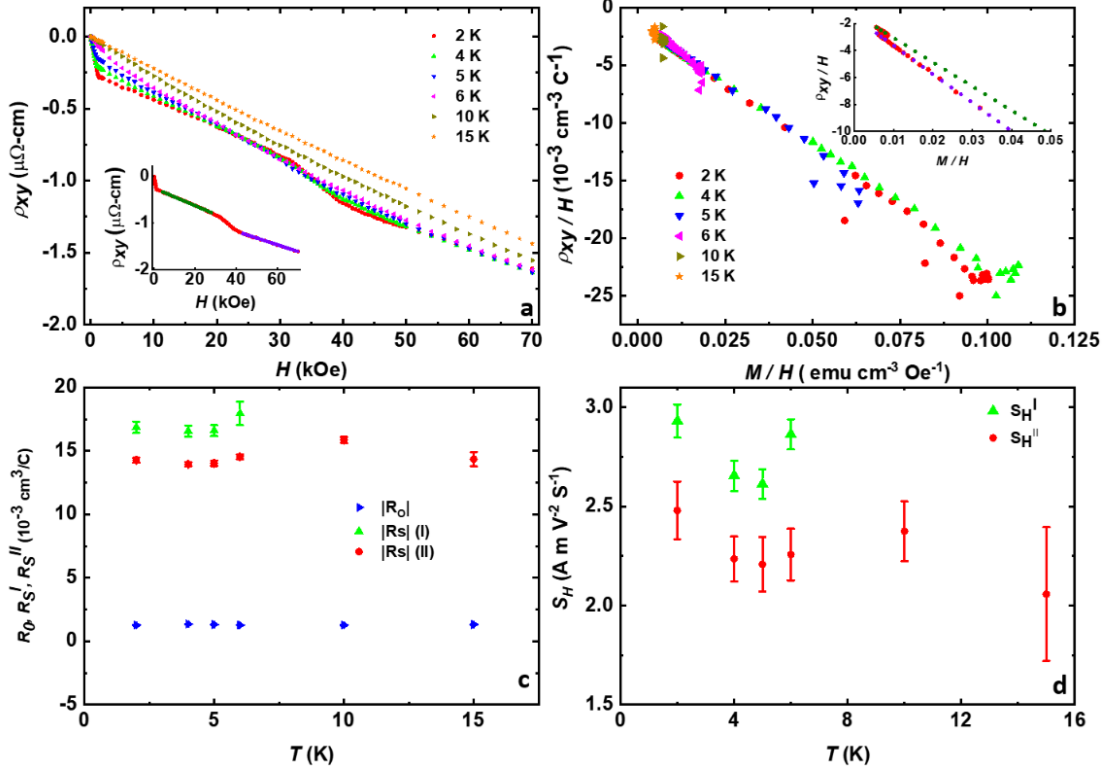


Fig. 5 Hall effect in NdAlGe. (a) Variation of Hall resistivity, ρ_{xy} , with the magnetic field, H at selected temperatures. The Hall resistivity was symmetrized to remove the effect of longitudinal resistivity. The inset shows variation of ρ_{xy} at $T = 2$ K. The $T = 2$ K data is fit with two linear regions (olive and violet) with different intercepts. (b) Variation of $\frac{\rho_{xy}}{H}$ with $\frac{M}{H}$ at select temperatures. Inset of (b) shows data at $T = 2$ K. The data at $T = 2$ K is fit with two linear regions with different slopes ($1 \text{ emu}/(\text{Oe cm}^3) = 4\pi$). (c) Variation of the magnitude of the ordinary (R_0) and anomalous (R_S^I and R_S^{II}) Hall coefficients with temperature. (d) Variation of the magnitude of the Hall conductivity parameter, S_H , with temperature.

The variation of $|R_0|$, $|R_S^I|$, and $|R_S^{II}|$ with temperature is plotted in Fig. 5c. It should be noted that the anomalous component, R_S , is almost 10 times larger than the ordinary component, R_0 , comparable to other compounds of this family [9,10,13,16]. The intrinsic or extrinsic contributions to the anomalous Hall effect can be deduced from the temperature dependence of the parameter S_H where $S_H = \frac{R_S}{\rho_{xx}^2}$. Fig. 5d shows the variation of S_H with T for the two different anomalous contributions. In the small range of temperature studied in this work, both S_H values seem relatively independent of the temperature. Given the large values of Hall

conductivities and the relative temperature-independent S_H , the anomalous Hall effect is likely to originate from the intrinsic Berry curvature-related phenomena [47,48]. We also analyzed the possibility of a topological Hall effect (in region I) and anomalous Hall effect in (in region II). These less likely scenarios are discussed in the discussion and conclusion sections.

3. e Neutron diffraction

The measurements of magnetization, heat capacity, and resistivity indicate two successive magnetic transitions at $T_{IC} = 6.3$ K and $T_C = 4.9$ K. To solve the magnetic structure of NdAlGe we have performed multiple neutron diffraction experiments. The results are presented in Fig. 6. In our first experiment, we solved the nuclear and magnetic structure at 4.8 K using HB-3A single-crystal diffractometer. A total of 127 nuclear peaks were used to solve the nuclear structure. The nuclear structure does not change with temperature and is the same as that at room temperature. From the refinement, the lattice parameters were found to be $a = b = 4.224$ Å and $c = 14.624$ Å at 4.8 K. The results of nuclear refinements at 4.8 K are presented in Table I and Appendix A.

We also performed single crystal neutron diffraction on HB-1A triple-axis spectrometer where we identified three magnetic wavevectors consistent with $\mathbf{k}_0 = (0, 0, 0)$, $\mathbf{k}_1 = (\frac{2}{3}, \frac{2}{3}, 0)$, and $\mathbf{k}_2 = (\frac{1}{3}, \frac{1}{3}, 0)$. The order parameters of each wavevector were measured at $\mathbf{Q} = (0, 2, 0)$, $(\frac{2}{3}, \frac{2}{3}, 0)$ and $(\frac{1}{3}, \frac{1}{3}, 0)$ using HB-1A triple axis spectrometer and are presented in Figs. 6b and 6c. The onset temperature of each order parameter i.e., $T_{IC} = 6.3$ K is consistent with the onset temperature observed in magnetization, resistivity, and heat capacity measurements. As will be discussed later, there is small incommensurability observed with \mathbf{k}_1 between $T_{IC} = 6.3$ K and $T_C = 4.9$ K.

Irreducible representation analysis was used to determine the symmetry-allowed magnetic structures for all 3 wavevectors. The analysis was performed using the program BASIREP [49] within the Fullprof software suite. There are two Nd atoms within the primitive unit cell at $\mathbf{r}_1 = (0, 0, 0)$ and $\mathbf{r}_2 = (\frac{1}{2}, 0, \frac{3}{4})$, and the basis vectors and refinable coefficients for each atom within the determined irreducible representation are shown in detail in Appendix C.

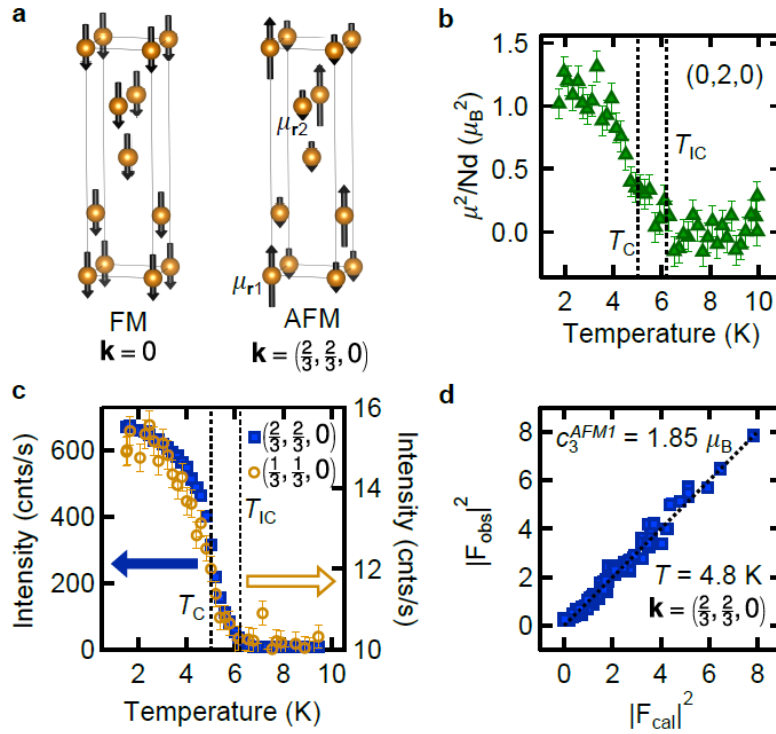


Fig. 6. (a) Schematic of $\mathbf{k}_0 = (0, 0, 0)$ FM and $\mathbf{k}_1 = (\frac{2}{3}, \frac{2}{3}, 0)$ (AFM1) magnetic structures in NdAlGe. For a phase of $\varphi^{\text{AFM1}} = 0$ and basis vector coefficient C_3^{AFM1} (see main text for details) the two-moment sizes in the AFM structure are $\mu_{r1} = C_3^{\text{AFM1}} \mu_B$ and $\mu_{r2} = -\frac{C_3^{\text{AFM1}}}{2} \mu_B$. (b) Order parameter for the $\mathbf{k}_0 = (0, 0, 0)$ FM component at $\mathbf{Q} = (0, 2, 0)$. The nuclear signal has been subtracted so all intensity is due to the magnetism, and the y-axis represents the evolution of the FM moment squared. (c) Order parameter for the $\mathbf{k}_1 = (\frac{2}{3}, \frac{2}{3}, 0)$ (filled blue squares, left axis) and $\mathbf{k}_2 = (\frac{1}{3}, \frac{1}{3}, 0)$ (open orange circles, right axis) AFM components of the NdAlGe magnetic structure, where data were taken at the $(\frac{2}{3}, \frac{2}{3}, 0)$ and $(\frac{1}{3}, \frac{1}{3}, 0)$ magnetic Bragg peaks, respectively. (d) Rietveld refinement results from HB-3A data taken at $\mathbf{G} + (\frac{2}{3}, \frac{2}{3}, 0)$ magnetic peak reflections at 4.8 K, where \mathbf{G} are allowed nuclear Bragg peak reflections. The black dashed line is $|F_{\text{cal}}|^2 = |F_{\text{obs}}|^2$.

There are three possible irreducible representations to describe the \mathbf{k}_0 structure: a c -axis FM structure (Γ_2), a c -axis AFM structure (Γ_4), or an in-plane FM or AFM structure (Γ_5). The in-plane structure (Γ_5) can be excluded due to the observation of $(0, 0, L)$ peaks having no magnetic intensity. Γ_4 can be excluded as well, as allowed $(H, 0, 0)$ and $(0, K, 0)$ reflections would yield zero intensity and as Fig. 6b shows, $(0, 2, 0)$ has magnetic intensity. Using the c -axis FM structure (Γ_2) shown in Fig. 6a, the moment—and refined coefficient, C_1^{FM} , for the FM component---was found to be $C_1^{FM} = -1.13(5) \mu_B$ close to the low field magnetization plateau at $0.95 \mu_B$. The evolution of the moment magnitude squared with decreasing temperature is shown in Fig. 6(b). The basis vectors for \mathbf{r}_1 and \mathbf{r}_2 within Γ_2 are shown in Table II.

Table II: Basis vectors and coefficients for the irreducible representation, Γ_2 for $\mathbf{k}_0 = (0, 0, 0)$. The last row shows the magnetic moment magnitude and orientation for each atom at \mathbf{r}_j

	$\mathbf{r}_1 = (0, 0, 0)$	$\mathbf{r}_2 = (\frac{1}{2}, 0, \frac{3}{4})$
Ψ_1	$C_1^{FM} (0, 0, 1)$	$C_1^{FM} (0, 0, 1)$
$\mu_{rj} = C_1^{FM} \hat{\mathbf{c}}$		

The magnetic structure with wavevector $\mathbf{k}_1 = (\frac{2}{3}, \frac{2}{3}, 0)$ was refined using data taken on HB-3A in four-circle mode at 4.8 K. A total of 100 magnetic reflections at $\mathbf{G} \pm (\frac{2}{3}, \frac{2}{3}, 0)$, where \mathbf{G} are the locations of allowed nuclear Bragg reflections, were used for refinement. There are two irreducible representations allowed (Γ_1 and Γ_2), where the moments at \mathbf{r}_1 and \mathbf{r}_2 are pointed in opposite directions. The basis vectors for \mathbf{r}_1 and \mathbf{r}_2 within Γ_2 are listed in Table III. The refinements led to c -axis only magnetic structure with coefficients $C_3^{AFM1} = 1.85 (1) \mu_B$ (at 4.8 K), which is shown in Fig. 6a along with refinement results in 6d. For a phase $\phi^{AFM1} = 0$, the distribution of moments from this structure leads to two different moment sizes of either C_3^{AFM1} or $\frac{C_3^{AFM1}}{2}$. This structure is similar to the magnetic structure of the sister compound

NdAlSi [8]. At 1.5 K, using the data taken from HB-3A in two-axis mode yields $C_3^{AFM1} = 3.8 (1) \mu_B$.

Table III: Basis vectors and coefficients for the irreducible representation, Γ_2 of \mathbf{k}_I . The last row shows the magnetic moment magnitude and orientation for each atom at \mathbf{r}_j , for the condition, $C_1^{AFM2} = C_2^{AFM2} = 0$.

	$\mathbf{r}_1 = (0, 0, 0)$	$\mathbf{r}_2 = (\frac{1}{2}, 0, \frac{3}{4})$
Ψ_1	$C_1^{AFM1} (1, 0, 0)$	$C_1^{AFM1} (0, -\frac{1}{2} - i\frac{\sqrt{3}}{2}, 0)$
Ψ_2	$C_2^{AFM1} (0, 1, 0)$	$C_2^{AFM1} (-\frac{1}{2} - i\frac{\sqrt{3}}{2}, 0, 0)$
Ψ_3	$C_3^{AFM1} (0, 0, 1)$	$C_3^{AFM1} (0, 0, -\frac{1}{2} - i\frac{\sqrt{3}}{2})$
$\boldsymbol{\mu}_{rj} = C_3^{AFM1} \cos [2\pi(\frac{2}{3}, \frac{2}{3}, 0) \cdot \mathbf{r}_j + \varphi^{AFM1}] \hat{\mathbf{c}}$		

We also observed weak magnetic peaks at $\mathbf{Q} = \pm(\frac{1}{3}, \frac{1}{3}, 0)$ similar to NdAlSi [8]. Because the (1, 1, 0) nuclear Bragg reflection is not allowed for space group $I4_1md$, these magnetic peaks cannot be stemming from the \mathbf{k}_I structure but are from an additional ordering in the magnetic structure with wavevector $\mathbf{k}_2 = (\frac{1}{3}, \frac{1}{3}, 0)$. There are not many $(\frac{1}{3}, \frac{1}{3}, 0)$ reflections that do not overlap with $(\frac{2}{3}, \frac{2}{3}, 0)$ -type reflections, and the data could be only taken at four such positions during our HB-1A experiment. The number of data points collected at $(\frac{1}{3}, \frac{1}{3}, 0)$ prevents full Rietveld refinement, however, some definitive conclusions can be drawn from the available data. Like \mathbf{k}_I , there are two irreducible representations (Γ_1 and Γ_2) allowed for \mathbf{k}_2 . Importantly, for Γ_1 , there would be no intensity at $\mathbf{Q} = \pm(\frac{1}{3}, \frac{1}{3}, 0)$, narrowing the irreducible representations to that of Γ_2 . Similarly, a c -axis only magnetic structure within Γ_2 , would result in zero intensity at $\mathbf{Q} = \pm(\frac{1}{3}, \frac{1}{3}, 0)$, so there must be some in-plane (ab -plane) component of the moment associated with $\mathbf{k}_2 = (\frac{1}{3}, \frac{1}{3}, 0)$ ordering.

The basis vectors for \mathbf{r}_1 and \mathbf{r}_2 within Γ_2 are presented in Table IV. If we assume the same in-plane magnetic structure as that of magnetic Weyl semimetal NdAlSi [8] ($C_1^{AFM2} = -C_2^{AFM2}$ and $C_3^{AFM2} = 0$), then moments point parallel or antiparallel to $[1, -1, 0]$ direction, and the moments at \mathbf{r}_1 and \mathbf{r}_2 are parallel to each other with values $\sqrt{2} C_1^{AFM2}$ and $\frac{\sqrt{2}}{2} C_1^{AFM2}$, respectively. We can then estimate the in-plane canting coefficient to be $C_1^{AFM2} = 0.136(7) \mu_B$, leading to in-plane moment magnitudes of either $0.19(1) \mu_B$ or $0.10(1) \mu_B$. These estimates come from the analysis of magnetic peaks collected at $\pm(\frac{1}{3}, \frac{1}{3}, 0)$, $(-\frac{1}{3}, \frac{2}{3}, 0)$, and $(\frac{2}{3}, -\frac{1}{3}, 0)$, which are at positions independent from reflections related to the \mathbf{k}_I magnetic structure.

Table IV: Basis vectors and coefficients for the irreducible representation, Γ_2 of \mathbf{k}_2 . The last row shows the magnetic moment magnitude and orientation for each atom at \mathbf{r}_j , for the condition, $C_1^{AFM2} = -C_2^{AFM2}$ and $C_3^{AFM2} = 0$.

	$\mathbf{r}_1 = (0, 0, 0)$	$\mathbf{r}_2 = (\frac{1}{2}, 0, \frac{3}{4})$
Ψ_1	$C_1^{AFM2} (1, 0, 0)$	$C_1^{AFM1} (0, -\frac{1}{2} + i\frac{\sqrt{3}}{2}, 0)$
Ψ_2	$C_2^{AFM2} (0, 1, 0)$	$C_2^{AFM1} (-\frac{1}{2} + i\frac{\sqrt{3}}{2}, 0, 0)$
Ψ_3	$C_3^{AFM2} (0, 0, 1)$	$C_3^{AFM1} (0, 0, -\frac{1}{2} + i\frac{\sqrt{3}}{2})$
$\boldsymbol{\mu}_{rj} = C_1^{AFM2} \cos [2\pi(\frac{1}{3}, \frac{1}{3}, 0) \cdot \mathbf{r}_j + \varphi^{AFM2}] (\hat{\mathbf{a}} - \hat{\mathbf{b}})$		

The total magnetic moment of each Nd is the sum of the \mathbf{k}_0 , \mathbf{k}_I , and \mathbf{k}_2 structures. Although the phase information (the parameters φ^{AFM1} and φ^{AFM2} as shown in Appendix C) is lost with neutron experiments, restraints based on the condition for constant moments can be made. These details are discussed fully in Appendix C. One constraint for constant moments independent of phases is that the ferromagnetic moment must be $|\frac{C_3^{AFM1}}{4}|$. It should be noted that during our refinement, we did not enforce this constraint, but that the value of the FM moment independently refined

to be close to this condition at $-0.3C_3^{AFM1}$. Assuming the perfect condition at $T = 1.5$ K, $C_1^{FM} = -\frac{C_3^{AFM1}}{4} = (-0.95 \mu_B)$, $C_3^{AFM} = 3.8 \mu_B$, and $C_1^{AFM2} = 0.136 \mu_B$, the constant moment condition would yield $2.85 \mu_B/\text{Nd}$ and agrees well with the high-field magnetization measurements.

3. f Incommensurate to Commensurate Transitions

Using the data from the WAND² experiment, we were able to resolve the small incommensurability associated with the \mathbf{k}_2 structure between T_{IC} and T_C . Data taken at $T_C < 5.5 \text{ K} < T_{IC}$, show magnetic Bragg peaks at positions $\mathbf{G} \pm (\frac{2}{3} + \delta, \frac{2}{3} + \delta, 0)$ and Fig. 7 shows the incommensurability. Figs. 7a and b are an H and K cut of the data, respectively, through the $(-2, -1, 1)$ Bragg peak position at 1.5 K, 5.5 K, and 9.0 K. Importantly, there is no observable shift in the peak position, although an increase in intensity is observed below 9.0 K as the \mathbf{k}_0 magnetic component increases. Figs. 7c and d are similar H and K cuts, but through the magnetic Bragg peak stemming from the $(-2, -1, 1)$ zone center. Here, a shift from the commensurate position of $(\delta, \delta, 0)$ is seen in the 5.5 K data. At this temperature, the shift is $\delta \approx 0.006 \text{ r.l.u.}$. Fig. 7 demonstrates the shift at one magnetic Bragg peak position, but it should be noted that this shift was observed for *all* magnetic Bragg peaks.

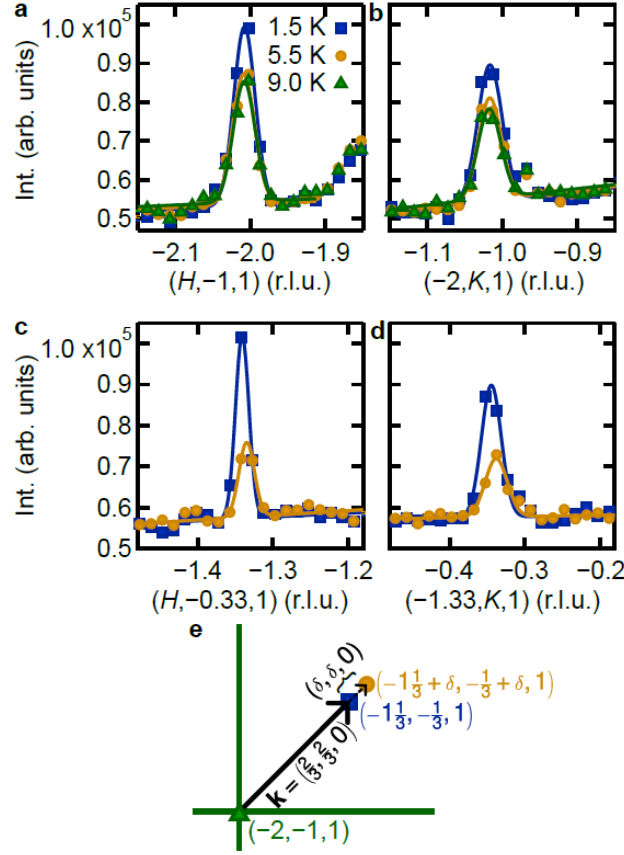


Fig. 7. Cuts through Bragg peaks from WAND² data. Integration about L is ± 0.4 r.l.u., and integration about H (for cuts along K) and K (for cuts along H) is ± 0.1 r.l.u. (a) H and (b) K cuts taken through the $(-2, -1, 1)$ Bragg peak at 9.0 K (green triangles), 5.5 K (blue squares), and 1.5 K (orange circles). These data show that no change in the peak position is observed as the temperature is lowered through T_C (6.3 K) and T_C (5 K). They also show the ferromagnetic $\mathbf{k}_0 = 0$ magnetic component via the increased intensity in the 5.5 K and 1.5 K data when compared to the 9 K data. (c) H and (d) K cuts through a magnetic Bragg peak at 5.5 K (orange circles) and 1.5 K (blue squares). A shift of $(\delta, \delta, 0)$ from the commensurate $(-1\frac{1}{3}, -1\frac{1}{3}, 0)$ position was observed in the 5.5 K data with $\delta = 0.006$ r.l.u. This shift was observed over all the antiferromagnetic magnetic Bragg peak positions within the detector range. (e) Schematic of the positions of the Bragg peaks shown in (a)-(d).

4. Electronic Structure Calculation

The NdAlGe cell was simulated in the fully polarized, or ferromagnetic (FM) state. Here, the Nd atoms are responsible for the magnetism of the structure, with the magnetic moment having negligible contributions from the Al and Ge atoms. In the

FM configuration, each Nd atom presents a magnetic moment equal to $2.96 \mu_B$. This value is similar to the average magnetic moment measured experimentally at $2.85 \mu_B$. The antiferromagnetic (AFM) and ferrimagnetic (FiM)-duu configurations are contrastingly more complex. Due to the complexity of both models, we only evaluated the FM structure. The FiM structure is characterized by a total magnetic moment different from zero. Similar results are expected if we apply the same analysis as the one reported here for the FM magnetic structure.

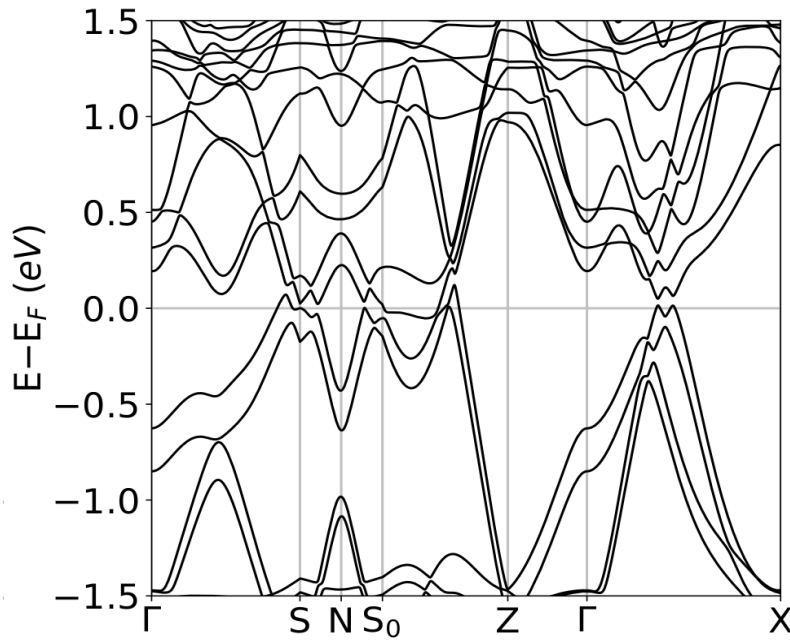


Fig. 8. Band diagram of the NdAlGe FM structure under the DFT+SOC+U framework.

Fig. 8 shows the band structure of the FM NdAlGe structure. The FM behavior is corroborated by noticing that there is always a significant gap between the bands that have the same slope, belonging to electrons with different spin states. It is worth mentioning that the addition of the +U functional pushes the region of high density of states away from the Fermi level leaving only a small number of Fermi surface band crossings. Additionally, Weyl points are clearly present in the trajectories Γ -S and Γ -X close to the Fermi level. This is further discussed below.

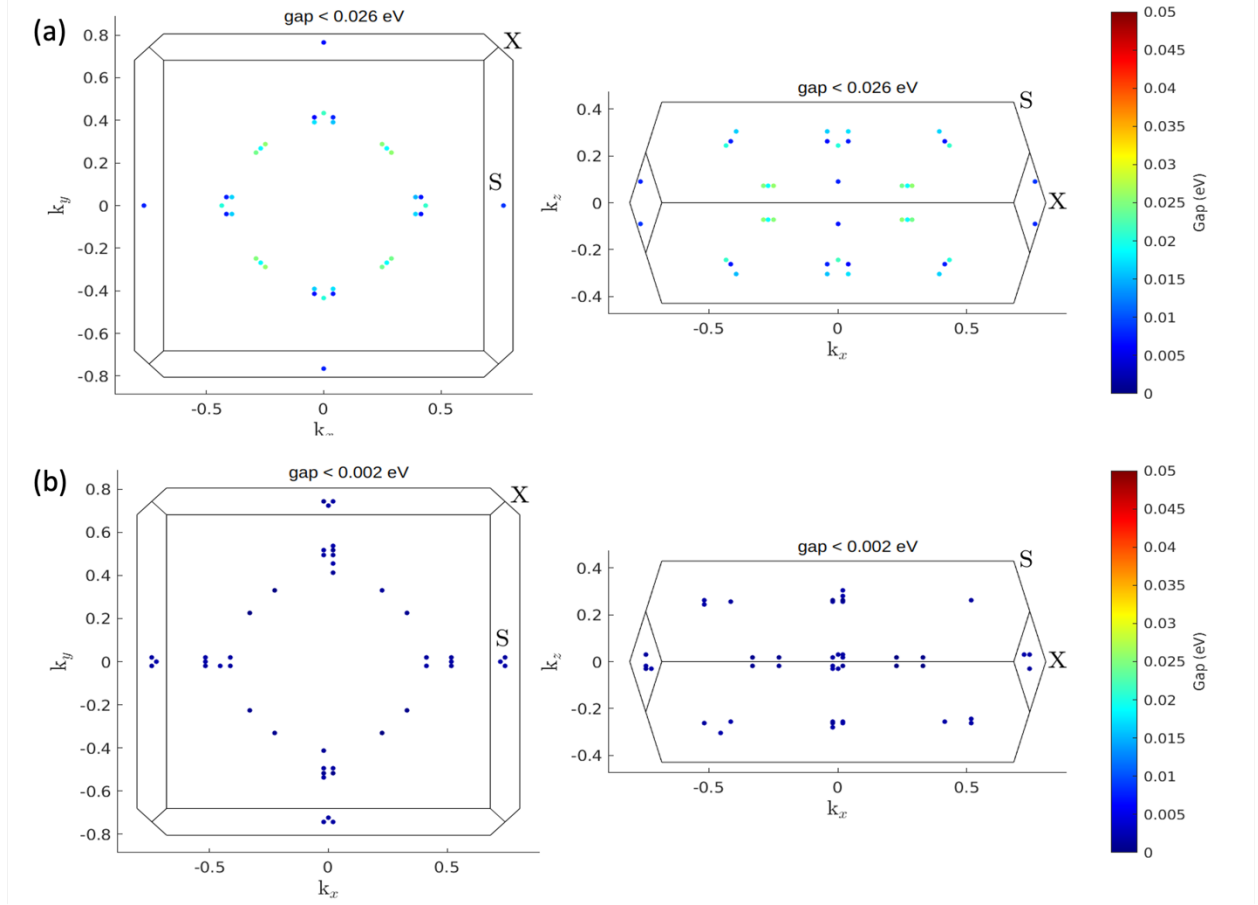


Fig. 9. Weyl nodes in the top (left) and front (right) views of the Brillouin zone with their respective energy gaps of DFT+U FM NdAlGe. Subfigures with a gap smaller than (a) 0.026 eV restrict the sign of the valence and conduction energies. Subfigure (b) removes this restriction and considers a gap smaller than 0.002 eV.

The determination of Weyl points is qualitatively easy. However, due to the approximate nature of the *ab-initio* calculations, a compromise between computational precision and physical exactitude must be made. More specifically, the quantitative determination of Weyl points in our calculations was done considering only the closest nodal points to the Fermi surface. To this end, the nodal points must have negative valence energy, positive conduction energy, and a gap smaller than a certain criterion between the two energies.

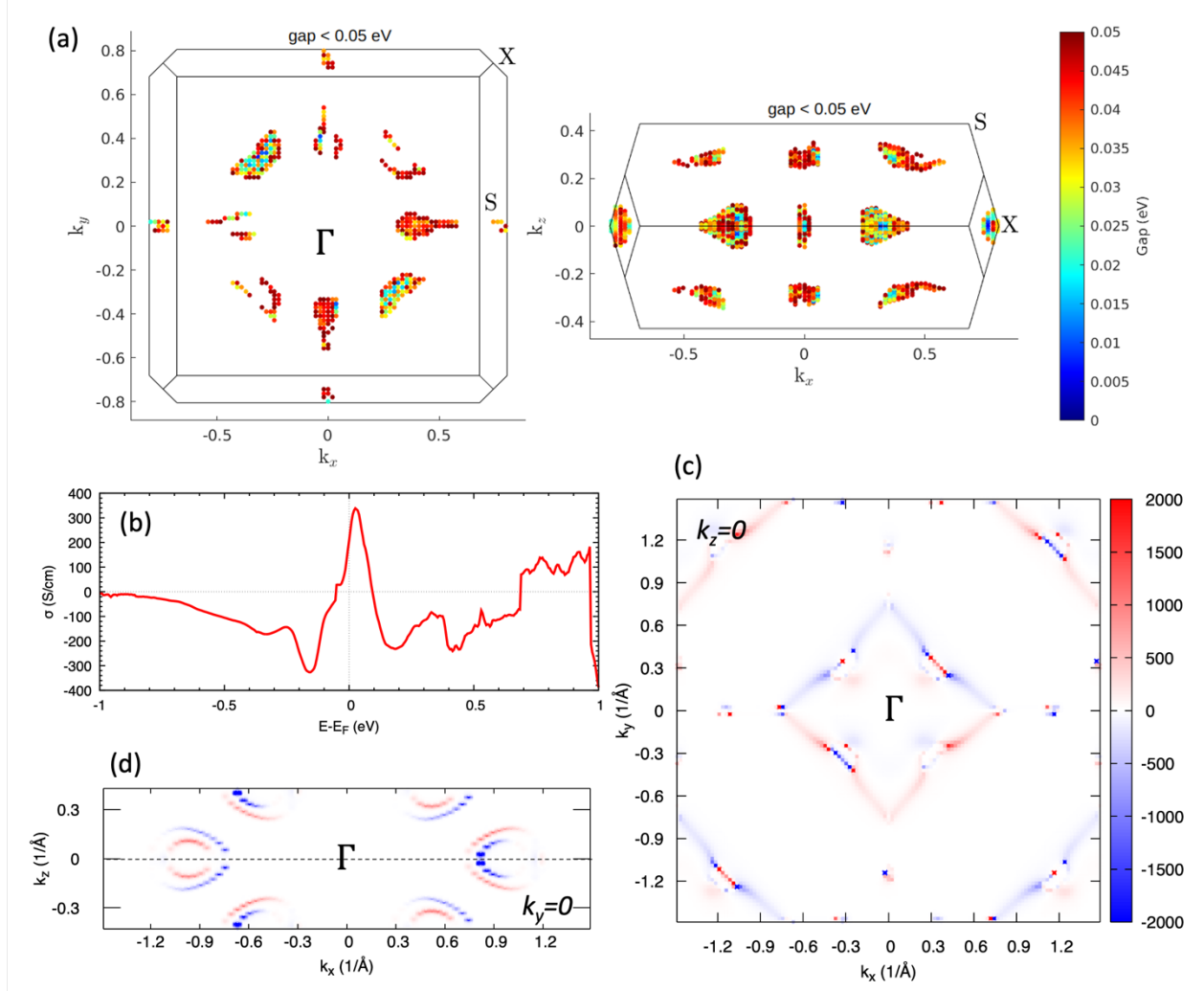


Fig.10. Weyl nodes in the top (left) and front (right) views with their respective energy gap from DFT+SOC+U FM NdAlGe. Subfigure (a) 0.05 eV without valence and conduction band restriction, (b) magnitude of the Anomalous Hall Conductivity as a function of energy. The Fermi energy is indicated by the dotted vertical line at zero energy, and the Berry curvature at 1 emu/(mol Oe) = $4\pi \cdot 10^{-6} \text{ m}^3/\text{mol}$. (c) $k_z = 0$ and (d) $k_y = 0$ planes depicting Weyl nodes as red/blue peaks at the Berry curvature.

In the DFT+U calculations, there are 48 Weyl points with a gap smaller than 0.019 eV and 70 Weyl points with a gap smaller than 0.026 eV. The former is the minimum gap in which Weyl points are observed along the Γ -X direction. See Figure 9a for a graphical representation of the points for a gap smaller than 0.026 eV in the Brillouin zone. If we remove the restriction on the signs of the band energies of the nodal points, then the gap is reduced to 0.002 eV. In this situation, there are a total of 72

Weyl points in the Brillouin zone (see Figure 9b). In all cases, the Weyl points are located around the Γ -S and Γ -X directions and are symmetric around Γ .

The addition of the SOC term in the Hamiltonian perturbs the system and prevents a quantitatively precise determination of the Weyl points. A greater value for the energy gap is necessary to obtain nodal points in the directions of interest. By considering a gap of 0.025 eV, there are 43 Weyl points in the Brillouin zone. By removing the restriction in the signs of the band energies, there are 72 Weyl points with a gap of 0.01 eV. Upon considering the highest threshold for the gap (0.05 eV, Figure 10a) the distribution of the Weyl points in the Brillouin zone begins to look like nodal surfaces and resemble the form of the Fermi surface.

We further calculate the anomalous Hall conductivity (Figure 10b) for the FM system setting the Fermi energy as reference. Our calculated value for $\sigma \approx 270 \Omega^{-1}\text{cm}^{-1}$ is in reasonable agreement with our experimental value ($\approx 430 \Omega^{-1}\text{cm}^{-1}$) in both order of magnitude and sign. As mentioned before, the large Anomalous Hall Conductivity is intrinsic due to the Berry curvature most likely generated by the Weyl points. To prove if the Weyl nodes generate such Berry curvature, we plot it at k -planes at the Weyl point positions. Figs. 10b and c depict the Berry curvature for $k_z = 0$ and for $k_y = 0$. These figures demonstrate that the Weyl points generate Berry curvature, which drives the intrinsic anomalous Hall effect already measured and confirmed by our electronic structure calculations. This effect likely appears because magnetism in Weyl semimetals modifies the Weyl nodes to induce a Berry curvature field, further generating several interesting phenomena such as the observed Anomalous Hall Effect.

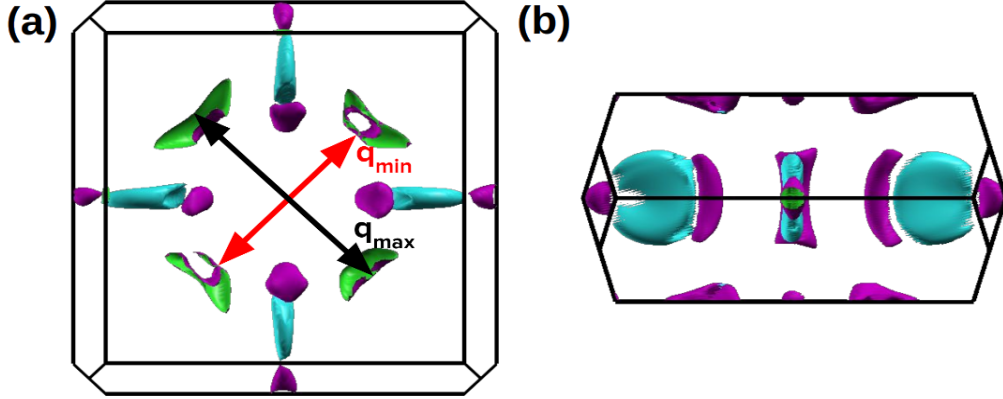


Fig. 11. Fermi surface and nesting vector in the DFT+SOC+U FM NdAlGe. (a) Shows a top view and (b) a front one.

Finally, Fig. 11 displays the Fermi surface of NdAlGe. Within this surface, we notice that the regions displayed in green in Fig. 11a are parallel to each other over a significant area. These are connected by the red and black nesting vectors drawn along the $[110]$ and $[1-10]$ directions. The lengths of the nesting vectors q_{min} and q_{max} are 0.63 \AA^{-1} and 0.80 \AA^{-1} , respectively.

5. Discussion and Conclusion

The two thermodynamic transitions observed in the resistivity, magnetic susceptibility, and heat capacity are related to the change in magnetic state from paramagnetic ($T > T_{IC}$) to incommensurate spin density wave state for $T_C \leq T \leq T_{IC}$ and to a commensurate ferrimagnetic state at $T \leq T_C$. The presence of both itinerant and local moments is inferred from the ratio of the effective moment (μ_{eff}) from Curie-Weiss law and the saturation magnetization (M_S) obtained from magnetization measurements at high magnetic fields and low temperatures. This ratio for NdAlGe is $\frac{\mu_{eff}}{M_S} = 1.2 > 1$, suggesting that the itinerant moments reduce the net saturation magnetization. The importance of the itinerant conducting carriers in determining the magnetism of NdAlGe is further supported by our electronic structure calculations where the calculated Fermi surface, shown in Fig. 11a, include small

hole pockets (green) near $\mathbf{Q} = \pm (\frac{1}{3}, \frac{1}{3}, l)$ that display well-nested surfaces. Typically, incommensurate spin density wave order in local moment systems, such as those involving rare earth ions, occurs via the RKKY interaction [50–52]. However, in a system such as NdAlGe the nested Fermi surfaces may affect the RKKY interactions between local moments creating an incommensurate spin density wave. In such a case, the magnetic wavevector for both the itinerant and local moments is set by the Fermi surface nesting condition. Such a scenario has been suggested in other rare earth compounds such as NdAlSi [8] and GdSi [51]. Since, in the case of NdAlGe, the nested pockets are Weyl like, and since the nesting vector determines the magnetic ordering vector, we conclude that the magnetism in NdAlGe is mediated by the itinerant Weyl fermions in a manner similar to that found in NdAlSi [8].

The magnetoresistance in NdAlGe also displays interesting behavior. As shown in Fig. 4 the magnetoresistance increases with field in the commensurate (uud) type-ferrimagnetic state (Region I), decreases in the transition region between I and II, and then reverses course with further increasing field having a positive MR in region II where the magnetic moments are in an (uuu) state. The magnetoresistance is large and increases by 15% for $H // c$ at $T = 0.4$ K and $H = 180$ kOe. The positive variation of magnetoresistance in the field polarized state is rather counterintuitive and may reflect a change in the electronic structure and Fermi surface topology as in other rare earth compounds such as NdAlSi [43] and heavy fermion metals [44,53]. Unfortunately, the disorder present in our sample ($\text{RRR} \approx 2.5$) prevents us from observing the quantum oscillations to further test this hypothesis. Future field-dependent magnetic and electronic structure analyses are required to fully understand the positive magnetoresistance in NdAlGe.

Our investigation of the Hall effect in NdAlGe revealed two unusual anomalous responses in the magnetic state. First, the anomalous Hall conductivity is

surprisingly large ($430 \text{ } \Omega^{-1} \text{ cm}^{-1}$, $T = 2 \text{ K}$, region I) and ($1030 \text{ } \Omega^{-1} \text{ cm}^{-1}$, $T = 2 \text{ K}$, region II). Such a large anomalous Hall conductivity cannot arise from an extrinsic skew scattering or side jump mechanism in NdAlGe with the conductivity lying within the dirty metal range. In fact, the obtained anomalous Hall conductivity in NdAlGe is of the same order of magnitude as the calculated intrinsic Berry curvature contribution from electronic structure and comparable to other members of this family [10,13]. Further, the presence of Weyl nodes near the Fermi surface and the large anomalous Hall response comparable to or greater than the intrinsic Berry curvature contribution limit indicates that the anomalous Hall effect in NdAlGe is caused by the large Berry curvature associated with the Weyl Fermions [46,54]. The two slightly different values of R_s are an indication of the electronic structure (and associated Berry curvature) modification with the field. This picture of electronic structure modification is also consistent with the positive magnetoresistance in region II. The large magnitude of the intrinsic anomalous Hall response which is related to the topology of electronic structure has also observed in other rare earth compounds such as DyPtBi [55], TbPtBi [56] and PrAlGe [13] giving us further confidence in our conclusion.

We also investigated the possibility of the presence of topological and anomalous (Berry phase related) Hall effects. In this scenario, there is only one anomalous Hall coefficient (R_S^{II}) which can be obtained by fitting the high field (region II) data in Fig. 5b. Any low field data (region I), that cannot be fitted with this large field anomalous Hall coefficient is the topological Hall effect (ρ_{xy}^T) arising from the non-trivial topology of magnetic structure in region I. Assuming such scenario, the variation of $\frac{\rho_{xy}^T}{H} = \frac{\rho_{xy}}{H} - R_0 - 4\pi R_S^{II} \frac{M}{H}$ is presented in Fig. 12. From Fig. 12, it appears that there is a large topological Hall effect in low field regime and the topological component disappears only in region II. The generation of such a large

topological Hall effect requires a highly non-collinear and non-coplanar magnetic structure. Our neutron diffraction experiments indicate an almost collinear (along c -axis) magnetic structure with only small ab -plane components. Such a magnetic structure is very unlikely to generate such a large topological Hall response.

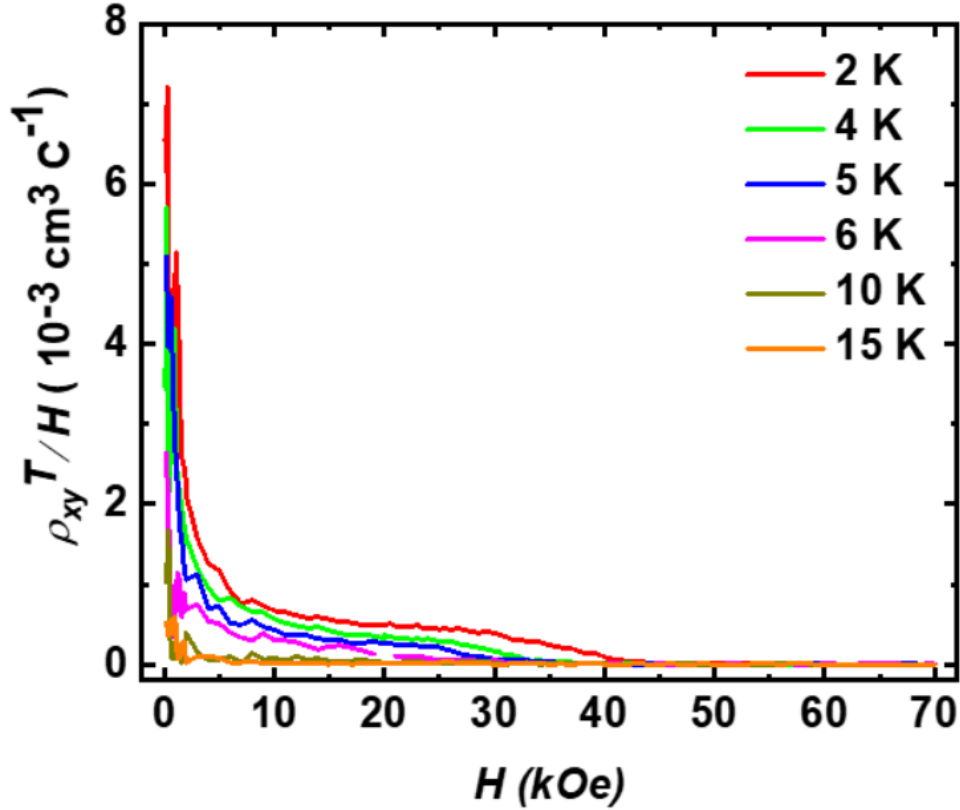


Fig. 12: Variation of $\frac{\rho_{xy}^T}{H}$ with H for NdAlGe at select temperatures.

In summary, our results indicate that the incommensurate spin density wave order and the large anomalous Hall response in NdAlGe are directly related to the nested Fermi surfaces containing Weyl nodes. The appearance of a multi- k structure along with a large anomalous Hall response is similar to what has been found in other compounds of this family. This establishes that the RAlX family of materials are good candidates to investigate the emergent electronic and magnetic properties arising from the interplay of itinerant Weyl fermions and local magnetic moments

and the possibility of controlling them through application of magnetic or electronic fields. Our work is pivotal in revealing the participation of relativistic fermions in controlling the collective behavior of materials such as magnetism. Future small-angle neutron scattering, and magnetic field-dependent neutron diffraction measurements are desired to understand the possibility of long-period topological magnetic phases and their evolution with magnetic fields and temperature.

Note: While preparing this manuscript similar results were reported in the preprint (<https://arxiv.org/pdf/2301.04893.pdf>) providing independent verification of our results.

Acknowledgments:

C. D acknowledges the helpful discussion with M. Asmar. This work is based upon the work supported by National Science Foundation under grant number DMR-2213443. The neutron diffraction experiments used resources at the High Flux Isotope Reactor, a DOE Office of Science User Facility operated by the Oak Ridge National Laboratory. A portion of this work was performed at the National High Magnetic Field Laboratory, which is supported by the National Science Foundation Cooperative Agreement No. DMR-1644779 and the State of Florida. The identification of any commercial product or trade name does not imply endorsement or recommendation by the National Institute of Standards and Technology. R.C and R. J are supported by the U.S. Department of Energy grant number DE- SC0012432. R.R, R.G and J.G acknowledge DGAPA-UNAM project IA100822 for partial financial support. Calculations were performed in the DGCTIC-UNAM Supercomputing Center project LANCADUNAM-DGTIC-368. JGS acknowledges A. Rodriguez-Guerrero for the technical support.

Appendix A: Crystal structure determination using single crystal and powder neutron diffraction.

We also performed single crystal neutron diffraction to determine the crystal structure at 4.8 K. The non-centrosymmetric structure and the variation of observed and calculated structure factors are shown in Fig. 13.

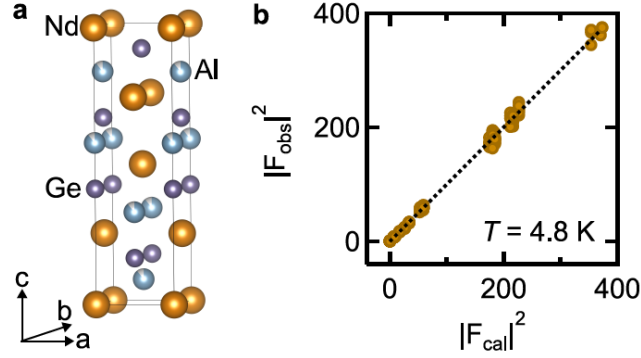


Fig. 13: (a) NdAlGe crystal structure with space group, $I4_1md$ (#109). (b) Rietveld refinement results for the nuclear structure taken at 4.8 K. Data are from single crystal neutron diffraction on HB-3A. Goodness of fit parameters can be found in Table I of the main text.

In addition to single crystal neutron diffraction, we also performed neutron powder diffraction on the polycrystalline sample prepared by arc melting and subsequent vacuum annealing at 1000 °C for 4 days. This is to ensure that this compound forms in non-centrosymmetric crystal structure despite slight variations in stoichiometry. We refined the same neutron data using both centrosymmetric ($I4_1/amd$) and non-centrosymmetric ($I4_1md$) space groups. The quality of refinement is much better with non-centrosymmetric structure.

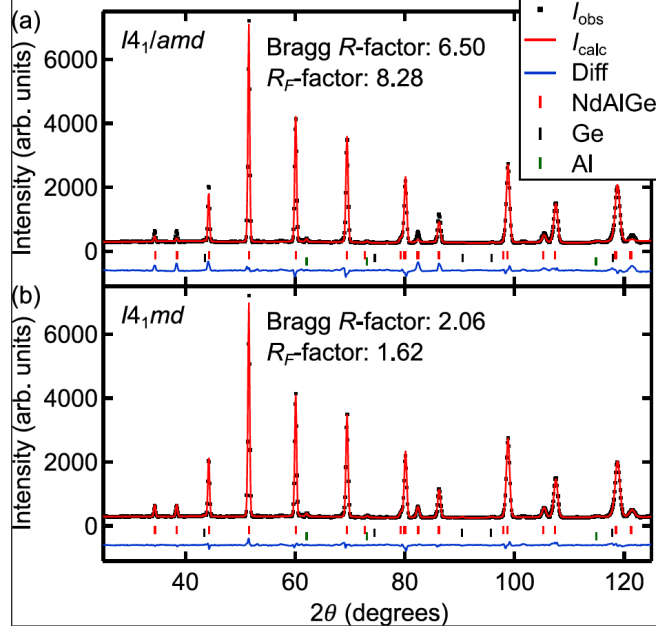


Fig. 14 Rietveld refinement of powder neutron pattern of NdAlGe at 20 K. (a) Using centrosymmetric ($I4_1/amd$) and, (b) using non-centrosymmetric ($I4_1md$) space groups. Goodness of fit parameters can be found in Table I of the main text.

Appendix B: Resistivity measurements

The resistivity was measured using four platinum electrodes mounted on the sample using silver epoxy. The current was applied along a axis.

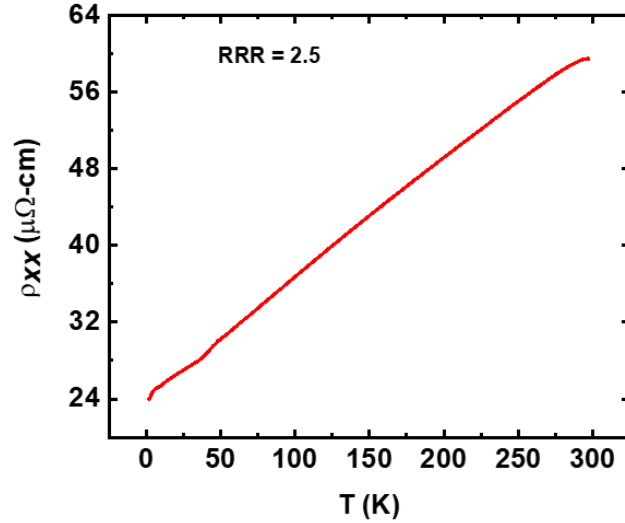


Fig. 15 Variation of longitudinal resistivity, ρ_{xx} , with temperature, T for NdAlGe.

Appendix C: Magnetic Structure Details

The arrangement of the Nd moments within NdAlGe is a sum of the \mathbf{k}_0 , \mathbf{k}_1 , and \mathbf{k}_2 magnetic structures. The sum must satisfy the condition that the total moment per Nd atom does not exceed $2.85 \mu_B$ as determined from high-field magnetization measurements. First consider only the \mathbf{k}_0 and \mathbf{k}_1 magnetic structure (no in-plane moment contribution from the \mathbf{k}_2 structure). A constant moment can only be achieved if $C_1^{FM} = \frac{C_3^{AFM1}}{4}$, where solutions exist for $C_1^{FM} = -\frac{C_3^{AFM1}}{4}$ and $\varphi^{AFM1} = \frac{2\pi}{3}n$ ($n = 0, 1, 2, \dots$) and for $C_1^{FM} = \frac{C_3^{AFM1}}{4}$, $\varphi^{AFM1} = \frac{2\pi}{3}\left(n + \frac{1}{2}\right)$ ($n = 0, 1, 2, \dots$). When considering a constant moment condition for \mathbf{k}_0 , \mathbf{k}_1 , and \mathbf{k}_2 , the same condition, $C_1^{FM} = \left|\frac{C_3^{AFM1}}{4}\right|$, still holds; however, to obtain a constant moment, one must solve for φ^{AFM1} and φ^{AFM2} solutions. Using the estimate, $C_1^{AFM2} = 0.136 \mu_B$, one solution is $\varphi^{AFM1} = 0.00085$ and $\varphi^{AFM2} = 0.78518$. Fig. 13 shows the evolution of these phase solutions as C_1^{AFM2} increases.

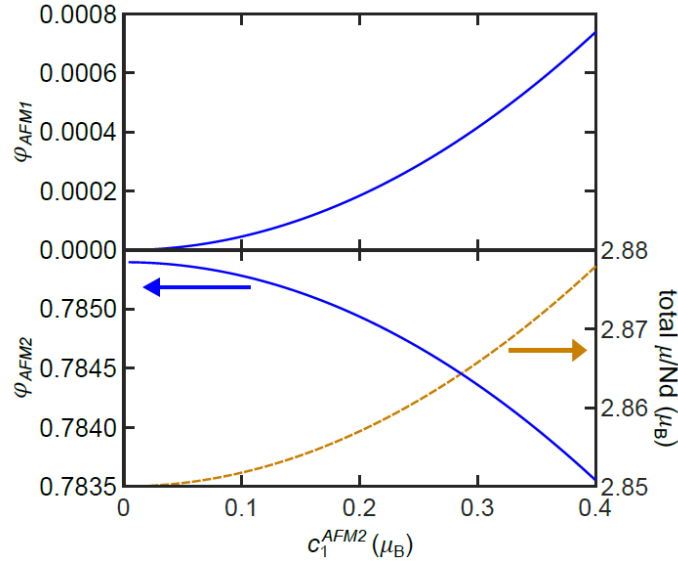


Fig. 16. Solutions for the phases φ^{AFM1} and φ^{AFM2} which result in each Nd atom having an equal moment. These solutions are for $C_3^{AFM1} = 3.8 \mu_B$ and $C_1^{FM} = -\frac{C_3^{AFM1}}{4} = -0.95 \mu_B$ and are plotted as a function of the coefficient C_1^{AFM2} . The left axis of top and bottom plots is the φ^{AFM1} and φ^{AFM2} solution, respectively, and the right axis of the bottom plot displays the total moment for each Nd as a function of C_1^{AFM2} .

Appendix D: Electronic structure calculations

The links for videos showing the appearance of nodal points with the band energies and gap criteria on the DFT+U and DFT+SOC+U are shown in this section:

DFT+U: https://drive.google.com/drive/folders/1TOjWP_mRT_jQ2aqq8s-QSU0Vik4sGmiO?usp=sharing

DFT+SOC+U: https://drive.google.com/drive/folders/1L1NBknRS32ZyVCSG75KmTyrDj_d6jhYj?usp=sharing

References

- [1] N. P. Armitage, E. J. Mele, and A. Vishwanath, *Weyl and Dirac Semimetals in Three-Dimensional Solids*, Rev. Mod. Phys. **90**, (2018).
- [2] M. Z. Hasan, G. Chang, I. Belopolski, G. Bian, S. Y. Xu, and J. X. Yin, *Weyl, Dirac and High-Fold Chiral Fermions in Topological Quantum Matter*, Nature Reviews Materials.
- [3] A. C. Potter, I. Kimchi, and A. Vishwanath, *Weyl and Dirac Semimetals*, Nat. Commun. **5**, 1 (2014).
- [4] L. Meng, J. Wu, Y. Li, and J. Zhong, *Dirac-Weyl Semimetal Phase in Noncentrosymmetric Transition Metal Monochalcogenides MoTe and WTe*, J. Mater. Chem. C **7**, 12151 (2019).
- [5] Z. X. Li, Y. Cao, and P. Yan, *Topological Insulators and Semimetals in Classical Magnetic Systems*, Physics Reports.
- [6] B. A. Bernevig, C. Felser, and H. Beidenkopf, *Progress and Prospects in Magnetic Topological Materials*, Nature.
- [7] D. S. Sanchez, G. Chang, I. Belopolski, H. Lu, J. X. Yin, N. Alidoust, X. Xu, T. A. Cochran, X. Zhang, Y. Bian, S. S. Zhang, Y. Y. Liu, J. Ma, G. Bian, H. Lin, S. Y. Xu, S. Jia, and M. Z. Hasan, *Observation of Weyl Fermions in a Magnetic Non-Centrosymmetric Crystal*, Nat. Commun. **11**, (2020).
- [8] J. Gaudet, H. Y. Yang, S. Baidya, B. Lu, G. Xu, Y. Zhao, J. A. Rodriguez-Rivera, C. M. Hoffmann, D. E. Graf, D. H. Torchinsky, P. Nikolić, D. Vanderbilt, F. Tafti, and C. L. Broholm, *Weyl-Mediated Helical Magnetism in NdAlSi*, Nat. Mater. **20**, 1650 (2021).
- [9] D. Destraz, L. Das, S. S. Tsirkin, Y. Xu, T. Neupert, J. Chang, A. Schilling,

- A. G. Grushin, J. Kohlbrecher, L. Keller, P. Puphal, E. Pomjakushina, and J. S. White, *Magnetism and Anomalous Transport in the Weyl Semimetal PrAlGe: Possible Route to Axial Gauge Fields*, Npj Quantum Mater. **5**, (2020).
- [10] P. Puphal, V. Pomjakushin, N. Kanazawa, V. Ukleev, D. J. Gawryluk, J. Ma, M. Naamneh, N. C. Plumb, L. Keller, R. Cubitt, E. Pomjakushina, and J. S. White, *Topological Magnetic Phase in the Candidate Weyl Semimetal CeAlGe*, Phys. Rev. Lett. **124**, 017202 (2020).
- [11] S. Y. Xu, N. Alidoust, G. Chang, H. Lu, B. Singh, I. Belopolski, D. S. Sanchez, X. Zhang, G. Bian, H. Zheng, M. A. Husanu, Y. Bian, S. M. Huang, C. H. Hsu, T. R. Chang, H. T. Jeng, A. Bansil, T. Neupert, V. N. Strocov, H. Lin, S. Jia, and M. Z. Hasan, *Discovery of Lorentz-Violating Type II Weyl Fermions in LaAlGe*, Sci. Adv. **3**, (2017).
- [12] P. Puphal, S. Krebber, E. Suard, R. Cubitt, C. Wang, T. Shang, V. Ukleev, J. S. White, and E. Pomjakushina, *Development of Magnetism in the Solid Solution of Ce1-XPrxAlGe: From Magnetic Topology to Spin Glass*, Phys. Rev. B **101**, (2020).
- [13] B. Meng, H. Wu, Y. Qiu, C. Wang, Y. Liu, Z. Xia, S. Yuan, H. Chang, and Z. Tian, *Large Anomalous Hall Effect in Ferromagnetic Weyl Semimetal Candidate PrAlGe*, APL Mater. **7**, (2019).
- [14] Y. Zhang, Y. Gao, X.-J. Gao, S. Lei, Z. Ni, J. S. Oh, J. Huang, S. Gorovikov, M. Hashimoto, D. Lu, J. Denlinger, R. J. Birgeneau, L. Wu, K. T. Law, E. Morosan, and M. Yi, *Kramers Nodal Lines and Weyl Fermions in SmAlSi*, (2022).
- [15] T. Suzuki, L. Savary, J. P. Liu, J. W. Lynn, L. Balents, and J. G. Checkelsky,

- Singular Angular Magnetoresistance in a Magnetic Nodal Semimetal*, Science (80-.). **365**, 377 (2019).
- [16] H.-Y. Yang, B. Singh, B. Lu, C.-Y. Huang, F. Bahrami, W.-C. Chiu, D. Graf, S.-M. Huang, B. Wang, H. Lin, D. Torchinsky, A. Bansil, and F. Tafti, *Transition from Intrinsic to Extrinsic Anomalous Hall Effect in the Ferromagnetic Weyl Semimetal $\text{PrAlGe}_{1-x}\text{Si}_x$* , APL Mater. **8**, 011111 (2020).
- [17] H.-Y. Yang, B. Singh, J. Gaudet, B. Lu, C.-Y. Huang, W.-C. Chiu, S.-M. Huang, B. Wang, F. Bahrami, B. Xu, J. Franklin, I. Sochnikov, D. E. Graf, G. Xu, Y. Zhao, C. M. Hoffman, H. Lin, D. H. Torchinsky, C. L. Broholm, A. Bansil, and F. Tafti, *Noncollinear Ferromagnetic Weyl Semimetal with Anisotropic Anomalous Hall Effect*, Phys. Rev. B **103**, 115143 (2021).
- [18] A. P. Sakhya, C.-Y. Huang, G. Dhakal, X.-J. Gao, S. Regmi, X. Yao, R. Smith, M. Sprague, B. Singh, H. Lin, S.-Y. Xu, F. Tafti, A. Bansil, and M. Neupane, *Observation of Fermi Arcs and Weyl Nodes in a Non-Centrosymmetric Magnetic Weyl Semimetal*, (2022).
- [19] K. Cho, W. H. Shon, K. Kim, J. Bae, J. Lee, C.-S. Park, S. Yoon, B. Cho, P. Rawat, and J.-S. Rhyee, *Anisotropic Metamagnetic Transition and Intrinsic Berry Curvature in Magnetic Weyl Semimetal NdAlGe* , SSRN Electron. J. (2022).
- [20] N. Kikugawa, T. Terashima, T. Kato, M. Hayashi, H. Yamaguchi, and S. Uji, *Bulk Physical Properties of a Magnetic Weyl Semimetal Candidate NdAlGe Grown by a Laser Floating-Zone Method*, Inorganics **11**, 20 (2023).
- [21] J. Zhao, W. Liu, A. Rahman, F. Meng, L. Ling, C. Xi, W. Tong, Y. Bai, Z. Tian, Y. Zhong, Y. Hu, L. Pi, L. Zhang, and Y. Zhang, *Field-Induced*

Tricritical Phenomenon and Magnetic Structures in Magnetic Weyl Semimetal Candidate NdAlGe, New J. Phys. **24**, (2022).

- [22] T. Wang, Y. Guo, C. Wang, and S. Yang, *Correlation between Non-Centrosymmetric Structure and Magnetic Properties in Weyl Semimetal NdAlGe*, Solid State Commun. **321**, (2020).
- [23] W. Cao, Y. Su, Q. Wang, C. Pei, L. Gao, Y. Zhao, C. Li, N. Yu, J. Wang, Z. Liu, Y. Chen, G. Li, J. Li, and Y. Qi, *Quantum Oscillations in Noncentrosymmetric Weyl Semimetal SmAlSi*, Chinese Phys. Lett. **39**, (2022).
- [24] G. Chang, B. Singh, S. Y. Xu, G. Bian, S. M. Huang, C. H. Hsu, I. Belopolski, N. Alidoust, D. S. Sanchez, H. Zheng, H. Lu, X. Zhang, Y. Bian, T. R. Chang, H. T. Jeng, A. Bansil, H. Hsu, S. Jia, T. Neupert, H. Lin, and M. Z. Hasan, *Magnetic and Noncentrosymmetric Weyl Fermion Semimetals in the R AlGe Family of Compounds (R= Rare Earth)*, Phys. Rev. B **97**, (2018).
- [25] H. Hodovanets, C. J. Eckberg, P. Y. Zavalij, H. Kim, W. C. Lin, M. Zic, D. J. Campbell, J. S. Higgins, and J. Paglione, *Single-Crystal Investigation of the Proposed Type-II Weyl Semimetal CeAlGe*, Phys. Rev. B **98**, (2018).
- [26] G. Kresse and J. Hafner, *Ab Initio Molecular Dynamics for Liquid Metals*, Phys. Rev. B **47**, 558 (1993).
- [27] G. Kresse and J. Furthmüller, *Efficiency of Ab-Initio Total Energy Calculations for Metals and Semiconductors Using a Plane-Wave Basis Set*, Comput. Mater. Sci. **6**, 15 (1996).
- [28] G. Kresse and J. Furthmüller, *Efficient Iterative Schemes for Ab Initio Total-Energy Calculations Using a Plane-Wave Basis Set*, Phys. Rev. B **54**, 11169 (1996).

- [29] J. P. Perdew, K. Burke, and M. Ernzerhof, *Generalized Gradient Approximation Made Simple*, Phys. Rev. Lett. **77**, 3865 (1996).
- [30] H. J. Monkhorst and J. D. Pack, *Special Points for Brillouin-Zone Integrations*, Phys. Rev. B **13**, 5188 (1976).
- [31] M. Methfessel and A. T. Paxton, *High-Precision Sampling for Brillouin-Zone Integration in Metals*, Phys. Rev. B **40**, 3616 (1989).
- [32] K. Momma and F. Izumi, *VESTA 3 for Three-Dimensional Visualization of Crystal, Volumetric and Morphology Data*, J. Appl. Crystallogr. **44**, 1272 (2011).
- [33] V. Wang, N. Xu, J.-C. Liu, G. Tang, and W.-T. Geng, *VASPKIT: A User-Friendly Interface Facilitating High-Throughput Computing and Analysis Using VASP Code*, Comput. Phys. Commun. **267**, 108033 (2021).
- [34] J. D. Hunter, *Matplotlib: A 2D Graphics Environment*, Comput. Sci. Eng. **9**, 90 (2007).
- [35] G. Pizzi, V. Vitale, R. Arita, S. Blügel, F. Freimuth, G. Géranton, M. Gibertini, D. Gresch, C. Johnson, T. Koretsune, J. Ibañez-Azpiroz, H. Lee, J.-M. Lihm, D. Marchand, A. Marrazzo, Y. Mokrousov, J. I. Mustafa, Y. Nohara, Y. Nomura, L. Paulatto, S. Poncé, T. Ponweiser, J. Qiao, F. Thöle, S. S. Tsirkin, M. Wierzbowska, N. Marzari, D. Vanderbilt, I. Souza, A. A. Mostofi, and J. R. Yates, *Wannier90 as a Community Code: New Features and Applications*, J. Phys. Condens. Matter **32**, 165902 (2020).
- [36] Q. Wu, S. Zhang, H.-F. Song, M. Troyer, and A. A. Soluyanov, *WannierTools: An Open-Source Software Package for Novel Topological Materials*, Comput. Phys. Commun. **224**, 405 (2018).

- [37] K. Klepp and E. Parthé, *R PtSi Phases (R = La, Ce, Pr, Nd, Sm and Gd) with an Ordered ThSi₂ Derivative Structure*, Acta Crystallogr. Sect. B Struct. Crystallogr. Cryst. Chem. **38**, 1105 (1982).
- [38] S. Bobev, P. H. Tobash, V. Fritsch, J. D. Thompson, M. F. Hundley, J. L. Sarrao, and Z. Fisk, *Ternary Rare-Earth Alumo-Silicides—Single-Crystal Growth from Al Flux, Structural and Physical Properties*, J. Solid State Chem. **178**, 2091 (2005).
- [39] S. Pukas, Y. Lutsyshyn, M. Manyako, and E. Gladyshevskii, *Crystal Structures of the RAlSi and RAlGe Compounds*, J. Alloys Compd. **367**, 162 (2004).
- [40] C. Kittel, *Introduction to Solid State Physics*, Eighth (2021).
- [41] J. H. Mendez, C. E. Ekuma, Y. Wu, B. W. Fulfer, J. C. Prestigiacomo, W. A. Shelton, M. Jarrell, J. Moreno, D. P. Young, P. W. Adams, A. Karki, R. Jin, J. Y. Chan, and J. F. DiTusa, *Competing Magnetic States, Disorder, and the Magnetic Character of Fe₃Ga₄*, Phys. Rev. B **91**, 144409 (2015).
- [42] B. Stebler, *The Resistivity Anomaly in Chromium Near the Néel Temperature*, Phys. Scr. **2**, 53 (1970).
- [43] J.-F. Wang, Q.-X. Dong, Z.-P. Guo, M. Lv, Y.-F. Huang, J.-S. Xiang, Z.-A. Ren, Z.-J. Wang, P.-J. Sun, G. Li, and G.-F. Chen, *NdAlSi: A Magnetic Weyl Semimetal Candidate with Rich Magnetic Phases and Atypical Transport Properties*, Phys. Rev. B **105**, 144435 (2022).
- [44] R. G. Goodrich, N. Harrison, and Z. Fisk, *Fermi Surface Changes across the Néel Phase Boundary of NdB₆*, Phys. Rev. Lett. **97**, 146404 (2006).
- [45] N. Nagaosa, J. Sinova, S. Onoda, A. H. MacDonald, and N. P. Ong,

Anomalous Hall Effect, Rev. Mod. Phys. **82**, 1539 (2010).

- [46] Y. Chen, D. L. Bergman, and A. A. Burkov, *Weyl Fermions and the Anomalous Hall Effect in Metallic Ferromagnets*, Phys. Rev. B - Condens. Matter Mater. Phys. **88**, (2013).
- [47] E. Liu, Y. Sun, N. Kumar, L. Muechler, A. Sun, L. Jiao, S.-Y. Yang, D. Liu, A. Liang, Q. Xu, J. Kroder, V. Süß, H. Borrmann, C. Shekhar, Z. Wang, C. Xi, W. Wang, W. Schnelle, S. Wirth, Y. Chen, S. T. B. Goennenwein, and C. Felser, *Giant Anomalous Hall Effect in a Ferromagnetic Kagome-Lattice Semimetal*, Nat. Phys. **14**, 1125 (2018).
- [48] A. K. Nayak, J. E. Fischer, Y. Sun, B. Yan, J. Karel, A. C. Komarek, C. Shekhar, N. Kumar, W. Schnelle, J. Kübler, C. Felser, and S. S. P. Parkin, *Large Anomalous Hall Effect Driven by a Nonvanishing Berry Curvature in the Noncolinear Antiferromagnet Mn_3Ge* , Sci. Adv. **2**, (2016).
- [49] J. Rodríguez-Carvajal, *Recent Advances in Magnetic Structure Determination by Neutron Powder Diffraction*, Phys. B Condens. Matter **192**, 55 (1993).
- [50] Y. Wu, Z. Ning, H. Cao, G. Cao, K. A. Benavides, S. Karna, G. T. McCandless, R. Jin, J. Y. Chan, W. A. Shelton, and J. F. DiTusa, *Spin Density Wave Instability in a Ferromagnet*, Sci. Rep. **8**, 5225 (2018).
- [51] Y. Feng, J. Wang, D. M. Silevitch, B. Mihaila, J. W. Kim, J.-Q. Yan, R. K. Schulze, N. Woo, A. Palmer, Y. Ren, J. van Wezel, P. B. Littlewood, and T. F. Rosenbaum, *Incommensurate Antiferromagnetism in a Pure Spin System via Cooperative Organization of Local and Itinerant Moments*, Proc. Natl. Acad. Sci. **110**, 3287 (2013).

- [52] A. Bhattacharyya, D. D. Khalyavin, F. Krüger, D. T. Adroja, A. M. Strydom, W. A. Kockelmann, and A. D. Hillier, *Incommensurate Spin-Density-Wave Antiferromagnetism in CeRu₂Al₂B* Phys. Rev. B **93**, 060410 (2016).
- [53] C. Capan, Y.-J. Jo, L. Balicas, R. G. Goodrich, J. F. DiTusa, I. Vekhter, T. P. Murphy, A. D. Bianchi, L. D. Pham, J. Y. Cho, J. Y. Chan, D. P. Young, and Z. Fisk, *Fermi Surface Evolution through a Heavy-Fermion Superconductor-to-Antiferromagnet Transition: De Haas–van Alphen Effect in Cd-Substituted CeCoIn₅*, Phys. Rev. B **82**, 035112 (2010).
- [54] D. Wawrzik, J.-S. You, J. I. Facio, J. van den Brink, and I. Sodemann, *Infinite Berry Curvature of Weyl Fermi Arcs*, Phys. Rev. Lett. **127**, 056601 (2021).
- [55] H. Zhang, Y. L. Zhu, Y. Qiu, W. Tian, H. B. Cao, Z. Q. Mao, and X. Ke, *Field-Induced Magnetic Phase Transitions and the Resultant Giant Anomalous Hall Effect in the Antiferromagnetic Half-Heusler Compound DyPtBi*, Phys. Rev. B **102**, 094424 (2020).
- [56] Y. Zhu, B. Singh, Y. Wang, C.-Y. Huang, W.-C. Chiu, B. Wang, D. Graf, Y. Zhang, H. Lin, J. Sun, A. Bansil, and Z. Mao, *Exceptionally Large Anomalous Hall Effect Due to Anticrossing of Spin-Split Bands in the Antiferromagnetic Half-Heusler Compound TbPtBi*, Phys. Rev. B **101**, 161105 (2020).

